Cell Reports
Medicine

Article

Catalytic neural stem cell exosomes for multi-stage targeting and synergistical therapy of retinal ischemia-reperfusion injury

Graphical abstract

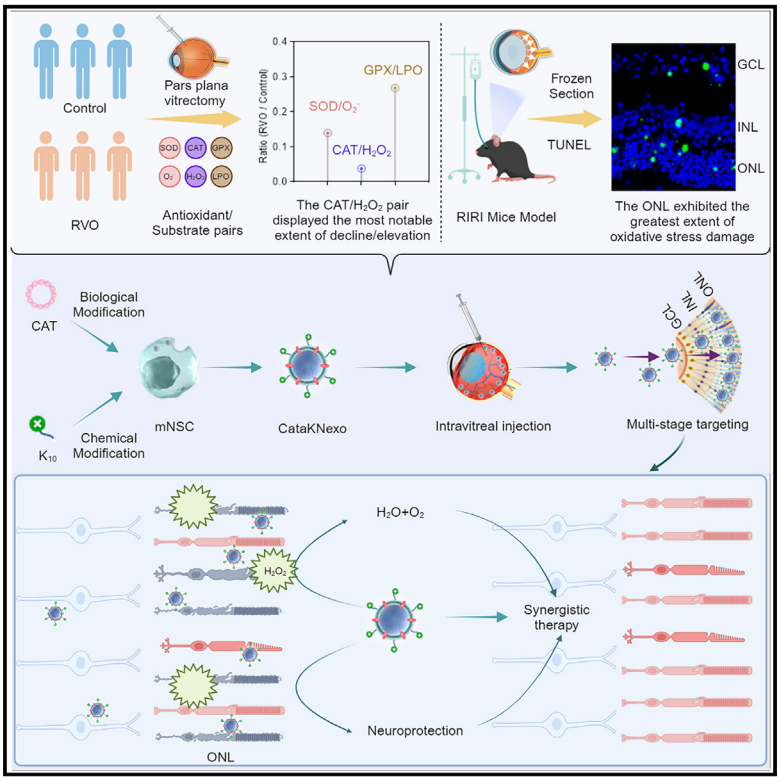

Highlights

- CAT/H_2O_2 pair exhibits the most significant oxidative dysregulation in RVO/RIRI
- ONL exhibits the most severe oxidative stress injury in RIRI models
- CataKNexo (K_{10}/catalase modified) reaches the ONL and exerts synergistic therapy
- CataKNexo prevents retinal cell death and exerts neuroprotection in RIRI models

Authors

Weiqiang Yang, Xiaojun Wang, Diwei Zheng, ..., Guanghui Ma, Wei Wei, Yong Tao

Correspondence

wangxiaojun@mail.ccmu.edu.cn (X.W.), ghma@ipe.ac.cn (G.M.), weiwei@ipe.ac.cn (W.W.), taoyong@mail.ccmu.edu.cn (Y.T.)

In brief

Building from the finding that the CAT/H_2O_2 dysregulation is most significant in RVO/RIRI and the ONL shows severe oxidative stress injury, Yang et al. develop a K_{10}-decorated and catalase-expressing exosome (CataKNexo). CataKNexo prevents H_2O_2-induced retinal cell death, exerts neuroprotection, and restores retinal function in RIRI mice and Bama miniature pigs.

Yang et al., 2025, Cell Reports Medicine 6, 102052
April 15, 2025
https://doi.org/10.1016/j.xcrm.2025.102052

CellPress

Cell Reports Medicine

CellPress
OPEN ACCESS

Article

Catalytic neural stem cell exosomes for multi-stage targeting and synergistical therapy of retinal ischemia-reperfusion injury

Weiqiang Yang,[1,2,3,8] Xiaojun Wang,[1,2,3,*] Diwei Zheng,[1,8] Jing Feng,[2,3] Wenjun Kong,[5] Yue Li,[1] Guanghui Ma,[1,3,4,*] Wei Wei,[1,3,4,*] and Yong Tao[2,3,6,7,9,*]

[1]State Key Laboratory of Biopharmaceutical Preparation and Delivery, Institute of Process Engineering, Chinese Academy of Sciences, Beijing 100190, P.R. China
[2]Department of Ophthalmology, Beijing Chaoyang Hospital, Capital Medical University, Beijing 100020, P.R. China
[3]Joint laboratory of Drug Delivery & Innovative Therapy built by Beijing Chaoyang Hospital & State Key Laboratory of Biopharmaceutical Preparation and Delivery, Institute of Process Engineering, Chinese Academy of Sciences, Beijing 100190, P.R. China
[4]School of Chemical Engineering, University of Chinese Academy of Sciences, Beijing 100049, P.R. China
[5]Department of Ophthalmology, Beijing You'an Hospital, Capital Medical University, Beijing 100069, P.R. China
[6]National Engineering Research Center for Ophthalmology, Beijing, P.R. China
[7]Engineering Research Center of Ophthalmic Equipment and Materials, Ministry of Education, Beijjing, P.R. China
[8]These authors contributed equally
[9]Lead contact
*Correspondence: wangxiaojun@mail.ccmu.edu.cn (X.W.), ghma@ipe.ac.cn (G.M.), weiwei@ipe.ac.cn (W.W.), taoyong@mail.ccmu.edu.cn (Y.T.)
https://doi.org/10.1016/j.xcrm.2025.102052

SUMMARY

Neuronal damage of the retina is a leading cause of visual impairment in patients with retinal ischemia-reperfusion injury (RIRI). Building on our clinical and experimental findings, the substantial decrease in catalase activity correlates with increased hydrogen peroxide (H_2O_2)-mediated oxidative stress that is primarily localized to the outer nuclear layer (ONL) situated in the posterior segment of the retina. Accordingly, we design a neural stem cell exosome with polylysine (K_{10}) decoration and catalase expression, named CataKNexo, which reaches the ONL and exerts synergistic antioxidant and neuroprotective therapy. Utilizing an *in vitro* retinal model recapitulating the layered architecture of the retina, we confirm that CataKNexo reaches the ONL through K_{10}-mediated transcytosis. In RIRI model mice, CataKNexo prevents the retina from H_2O_2-induced cell death, exerts neuroprotection, and restores vision function to near-normal levels. Moreover, CataKNexo shows promising antioxidative, neuroprotective, and safety profiles in RIRI model Bama miniature pigs, highlighting its potential for clinical translation.

INTRODUCTION

Retinal ischemia-reperfusion (IR) is a typical pathophysiological process of retinal vein occlusion (RVO) and other retinal ischemic diseases that deleteriously affect the visual health of an estimated 400 million patients worldwide.[1–5] To date, oxidative stress has been considered as causative factor for retinal IR-induced injury, which drives to intracellular reactive oxygen species (ROS) generation and antioxidant capacity imbalance.[6,7] Despite the use of various symptomatic treatments in clinical practice, there is currently no effective therapy for the preservation of vision in patients with retinal IR-induced injury. For example, retinal laser photocoagulation, which has been used to treat retinopathy for 50 years, fails to directly address the biological essence of elevated ROS levels, yielding limited efficacy and potentially resulting in retinal scotoma.[8,9] Therefore, an etiological strategy is urgently needed to counteract oxidative stress, repair cellular damage, and protect the visual function of patients.

Previous investigations have established the advantages of stem cells in treating IR-related conditions, such as ischemic stroke and myocardial infarction.[10–12] Nonetheless, the direct therapeutic use of stem cells in ocular diseases is subject to certain limitations, including a short survival time, phenotypic alterations, and abnormal proliferation.[13,14] Exosomes, emanating from parent cells, present a promising alternative to stem cells owing to their stable status and incorporation of active constituents such as microRNA (miRNA), proteins, and many other signal molecules.[15–18] Given that neurons are the primary cells damaged in retinal IR injury (RIRI),[19] exosomes derived from neural stem cells (NSCs), denoted as Nexo, have potential benefits of accumulating to the retina via targeting receptor on the membrane and reducing neuronal damage by neuroprotective components in vesicles.[20–22] Additionally, recent advances in synthetic biology have inspired Nexo modifications that enable them to effectively combat oxidative stress by expressing antioxidase.[23–25]

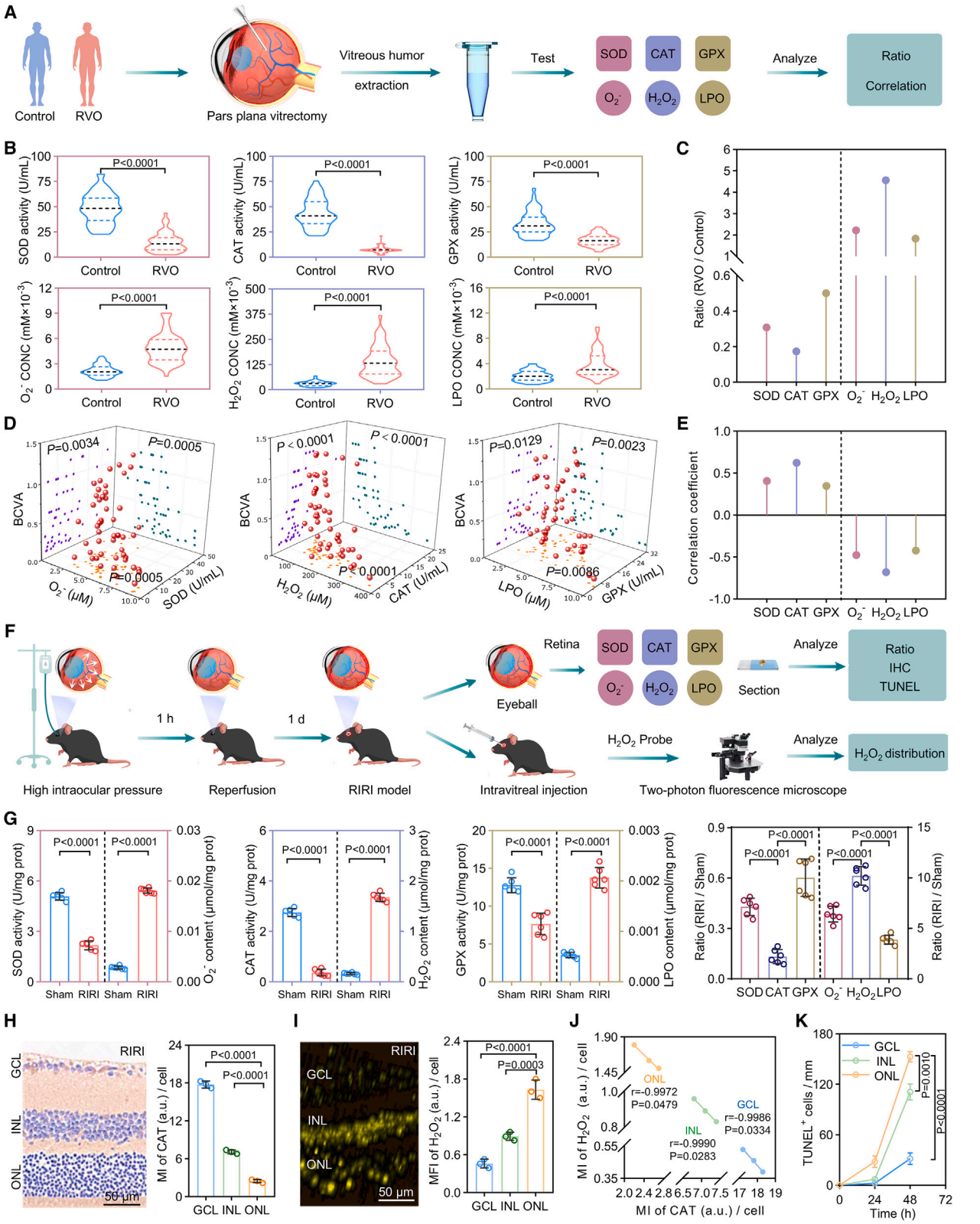

(legend on next page)

While Nexo represent a promising therapeutic chassis, two critical issues must be addressed before applying our technology. First, by analyzing the expression of various antioxidant enzymes in the Human Protein Atlas database, we selected the top three enzymes for further study: superoxide dismutase (SOD), catalase (CAT), and glutathione peroxidase (GPX), along with their corresponding substrates: superoxide anion (O_2^-), hydrogen peroxide (H_2O_2), and lipid peroxide (LPO).[26–28] Second, the retina comprises three nuclear layers (ganglion cell layer [GCL], inner nuclear layer [INL], and outer nuclear layer [ONL]), and different retinal sites exhibit varying degrees of resistance to IR injury.[29,30] Precise drug delivery to the specific structure that exhibits the most prominent injury could improve therapeutic efficacy.

In this study, we examined three major antioxidant/substrate pairs in patients with RVO (a typical RIRI disease) and relevant controls, which determined that the CAT/H_2O_2 pair displayed the most pronounced extent of oxidative dysregulation and correlation with illness severity.[31] In the classic RIRI mouse model, in addition to confirming the dominant role of the CAT/H_2O_2 pair in precipitating oxidative dysregulation, we further found that the ONL in oculi fundus exhibited the greatest extent of neuronal damage source from the oxidative stress. These two pathological findings indicate the necessity of endowing Nexo with additional CAT activity for ROS scavenging and deeper penetration into the ONL. Accordingly, we displayed CAT and conjugated polylysine (K_{10}) on the Nexo surface, resulting in CataKNexo. Following intravitreal injection, CataKNexo initially accumulates in the retina through receptor ligand recognition and then penetrates to the ONL via lysine-mediated transcytosis.[32,33] Furthermore, the CAT component scavenges H_2O_2 to combat oxidative stress, while the neuroprotective components alleviate neuronal damage, leading to therapeutic benefits against retinal IR injury. Consequently, CataKNexo confers strong therapeutic benefits with few abnormalities in RIRI model mice and pigs, highlighting their promise as safe and efficient therapeutics for treating RIRI-related diseases.

RESULTS

Aberrant CAT activity in the ONL is a prominent pathological feature of RIRI

Retinal IR is a pathophysiological process that drives an extensive increase in ROS, which contributes to the cellular damage observed in RVO.[34] Although previous clinical reports have shown dysregulated ROS levels in RVO, we are unaware of any studies examining which antioxidant enzymes may contribute to this oxidative stress.[35] By literature search[36–38] and analysis of the expression of various antioxidant enzymes in the Human Protein Atlas database, we selected the three representative enzymes for further study: SOD, CAT, and GPX, along with their corresponding substrates: O_2^-, H_2O_2, and LPO. Here, we investigated the activities of three antioxidant enzymes in vitreous humor samples from an RVO cohort (n = 50) and control patients with retinal diseases lacking IR (idiopathic macular epiretinal membrane, or idiopathic macular hole; n = 50) (Figure 1A). Briefly, the antioxidant activities of all tested enzymes were each significantly decreased in the RVO cohort compared to the control group, whereas the concentrations of their substrates were all significantly increased (Figure 1B), with the CAT/H_2O_2 pair revealing the most pronounced imbalance in the RVO cohort (Figure 1C). Further taking disease severity of the RVO cohort into consideration, we obtained best-corrected visual acuity (BCVA) index data and discovered that the CAT/H_2O_2 pair was most strongly correlated with severity (Figures 1D and 1E; Figure S1A).

Figure 1. Aberrant CAT activity and H_2O_2 accumulation in the retinal ONL are prominent pathological features of RIRI

(A) Schematic for extraction of the vitreous humor and subsequent analyses of antioxidase activities (SOD, CAT, and GPX) and ROS accumulation (O_2^-, H_2O_2, and LPO) in the RVO group (50 patients with retinal vein occlusion, a typical RIRI disease) and control group (50 patients with idiopathic macular epiretinal membrane or idiopathic macular hole).

(B) Measurement of antioxidant activities and ROS concentrations in the vitreous humor using Micro Antioxidase Activity Assay Kits and ROS Content Assay Kits. Control: n = 50 (1 eye from each of 50 patients); RVO: n = 50 (1 eye from each of 50 patients).

(C) Ratios of mean antioxidase activities and ROS concentrations between the RVO and control group.

(D) Spearman's rank correlation analyses examining relationships among antioxidase activities, ROS concentrations, and BCVA in patients with RVO (n = 50). Each red dot represents a vitreous humor sample extracted from an individual patient's eye. The XY plane (orange dots) represents the negative correlation values from an analysis between the antioxidase activity and ROS concentration. The XZ plane (cyan dots) represents the positive correlation values between ROS and BCVA. The YZ plane (purple dots) represents the negative correlation values between antioxidase activity and BCVA.

(E) Correlation coefficients of BCVA with antioxidase activities and ROS concentrations in the RVO group.

(F) Schematic for the extraction of retina and subsequent assays for antioxidase activities and ROS accumulation, as well as the accumulation of H_2O_2 in sham and RIRI model mice (sham: only the needle was inserted into the anterior chamber without saline infusion; RIRI model: retinal ischemia was induced by the instillation of saline into the anterior chamber of mice for 1 h, and then the high pressure was removed to restore perfusion of the retina).

(G) Measurement of antioxidase activities (SOD, CAT, and GPX) and ROS concentrations (O_2^-, H_2O_2, and LPO) in retinal samples of mice (left). Ratios of the mean antioxidase activities and mean ROS concentrations between the sham and RIRI model mice (right) (n = 6, 1 eye from each of 6 mice).

(H) Representative images of CAT immunostaining and quantitative analysis of the expression of CAT in histological sections of retinas from RIRI model mice (n = 3, 1 eye from each of 3 mice). Scale bar: 50 μm.

(I) Representative image from a two-photon fluorescence microscopy analysis of H_2O_2 and quantitative analysis of H_2O_2 accumulation in the GCL, INL, and ONL of retinas from RIRI model mice (n = 3, 1 eye from each of 3 mice). Scale bar: 50 μm.

(J) Spearman's rank correlation analyses examining relationships between CAT expression and H_2O_2 accumulation in the GCL, INL, and ONL of retinas from RIRI model mice (n = 3, 1 eye from each of 3 mice).

(K) Quantitative analysis of the extent of cell injury in three retinal layers from RIRI model mice at the indicated time points (n = 3 biologically independent experiments).

Data in (B) are presented as medians (25th–75th quartiles) and were compared using Mann-Whitney U test. Data in (G), (H), (I), and (K) are mean ± SD and were compared using one-way ANOVA. The experiments in (H) and (I) were independently repeated three times with similar results. See also Figure S1.

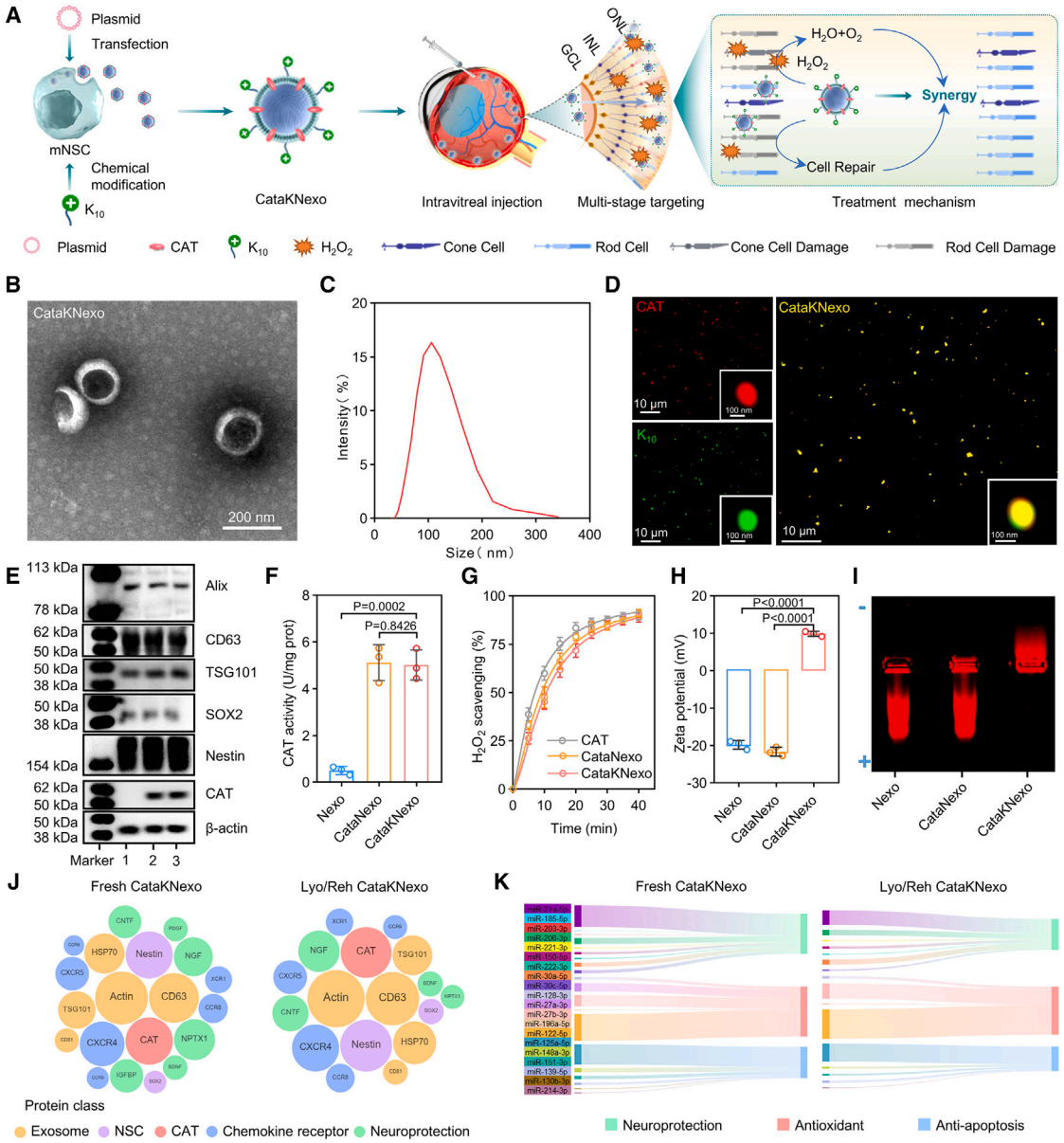

Figure 2. Construction and characterization of CataKNexo

(A) Schematic of the construction of CataKNexo and the combination of scavenging H_2O_2 with repairing cell damage. CataNexo are derived from mNSC (mouse neural stem cells) transfected with CAT-expressing lentiviral vectors (pLVX-CD63-CAT) and subsequently conjugated with K_{10} on the membrane. Among them, CD63 fusion protein can ensure the expression of CAT on the membrane. Wherein, CataKNexo collaboratively reduce the H_2O_2 accumulation and oxidative stress injury based on the effect of CAT and neurotrophic factors and functional miRNAs.

(B) TEM image of CataKNexo stained with uranyl acetate. Scale bar: 200 nm.

(C) Nanoparticle tracking analysis (NTA) of CataKNexo.

(D) CLSM images of CataKNexo showing co-localization of CAT (Cy3 labeled, red) and K_{10} (FITC labeled, green). The insets are STED images of the outlined region in the main images. The images (scale bar: 10 μm) and insets on the right (scale bar: 100 nm) are presented with same magnification, respectively.

(E) Immunoblotting of Nexo (1), CataNexo (2), and CataKNexo (3) with β-actin as control. Alix, CD63, and TSG101 are exosome markers. SOX2 and Nestin are NSC exosome markers. CAT is an expressed protein of CataNexo and CataKNexo.

(F) CAT activities of Nexo, CataNexo, and CataKNexo using a Micro CAT Assay Kit (n = 3 biologically independent experiments).

(G) H_2O_2 scavenging efficiency of CataNexo and CataKNexo compared to commercial CAT (EC 1.11.1.6) (n = 3 biologically independent experiments).

(H) Zeta potentials of Nexo, CataNexo, and CataKNexo (n = 3 biologically independent experiments).

(I) Agarose gel electrophoresis image of Nexo, CataNexo, and CataKNexo.

(legend continued on next page)

To test whether the aforementioned pathological features exhibited a similar trend in an animal model, we leveraged a well-established murine model of RIRI by raising the intraocular pressure to 110 mm Hg for 60 min, with sham surgical mice used as controls (Figure 1F; Figure S1B). Once again, we observed that the CAT/H_2O_2 pair displayed the most notable extent of decline/elevation (Figure 1G). Given that the primary structure of the retina consists of three nuclear layers with spatial heterogeneity,[39] we further wondered whether there were any differences in the CAT and H_2O_2 levels, as well as cellular injury, across these layers. To this end, we performed fluorescence staining to investigate the distribution of CAT and H_2O_2 in the retinas of RIRI model mice. Briefly, the ONL of the RIRI model mice presented the lowest CAT expression and the highest H_2O_2 production (Figures 1H–1J), indicating that oxidative stress damage occurred most prominently in the ONL. Therefore, we further conducted retinal cell apoptosis staining of RIRI model mice and found that cell damage indeed occurred most obviously in the ONL (Figure 1K; Figure S1C). These spatially inclined results from the RVO cohort and RIRI model mice sparked our inspiration in designing the treatment strategy of prioritizing the ONL for CAT delivery and neuron repair.

Construction and characterization of CataKNexo

For therapeutic purposes, we initially utilized Nexo as a chassis due to the aforementioned benefits of accumulating to the retina, reducing neuronal damage, and ability to display antioxidase. Beyond this, we also proposed that the conjugation of a specific component could endow Nexo with the capacity of deeper penetration to ONL. Keeping this in mind, we employed sequential biological-chemical modifications to develop CataKNexo (Figure 2A). To ensure the surface display of CAT, we fused CAT with membrane protein CD63 and transfected a lentivirus (pLVX-CD63-CAT) into mouse NSCs (mNSCs) (Figures S2A and S2B). Exosomes displaying CAT (CataNexo) were harvested from these cells using differential ultracentrifugation. Subsequently, K_{10} peptides were conjugated on the CataNexo surface using a condensation reaction of amino and carboxyl groups, resulting in our CataKNexo therapeutic. Upon intraocular injection, we envisioned that CataKNexo could reach the ONL and provide synergistic therapy via effective antioxidation and neuroprotection.

Transmission electron microscopy (TEM) analysis of CataKNexo revealed a cup-like morphology, and CataKNexo had particle sizes ranging from 50 to 200 nm (Figures 2B and 2C). Further supporting the successful surface dual modification, the CAT signal highly colocalized with lysine signal in confocal laser scanning microscopy (CLSM) and inserted stimulated emission depletion (STED) images (Figure 2D). For further verification, we compared CataKNexo with their exosomal counterparts (Nexo and CataNexo). Immunoblotting revealed that Nexo, CataNexo, and CataKNexo all contained markers for exosomes (Alix, CD63, and TSG101) and NSCs (SOX2 and Nestin), whereas signals for CAT were detected only in the CataNexo and CataKNexo samples (Figure 2E; Figure S2C). The CAT displayed on the Nexo and KNexo also maintained high activity (Figure 2F), with the H_2O_2 scavenging efficiency of CataNexo and CataKNexo much similar to that of pristine CAT (Figure 2G). In addition, the mean zeta potential of CataKNexo increased from −20 (Nexo and CataNexo) to 10 mV (Figure 2H), and CataKNexo but neither Nexo nor CataNexo migrated toward the negative pole in an agarose gel electrophoresis (Figure 2I), again supporting the presence of positively charged K_{10}. Finally, CataKNexo demonstrated favorable biological stability and storage characteristics, with no detectable changes in particle size or zeta potential after incubation in the vitreous humor at 37°C for 7 days, in PBS at 4°C for 21 days, or after lyophilization/rehydration (Lyo/Reh) (Figures S2D–S2F). Notably, proteomic analysis of CataKNexo, both in the fresh state and after Lyo/Reh, revealed comparable abundances of characteristic proteins related to exosomes, NSCs, chemokine receptors, neuroprotection, and CAT expression (Figure 2J). miRNA sequencing also revealed that fresh and Lyo/Reh CataKNexo shared representative miRNAs related to antioxidant, neuroprotection, and anti-apoptosis (Figure 2K). Such satisfactory storage stability renders CataKNexo available for potential applications as off-the-shelf products that can be used in an acute setting for RVO.

Prolonged retention and multi-stage targeting of CataKNexo in RIRI model mice

After intravitreal injection of CataKNexo into the eyes of RIRI model mice, we next investigated the spatiotemporal characteristics of CataKNexo (Figure 3A). Initially, we evaluated the retention of cyanine 5 NHS ester (Cy5-SE)-labeled exosomes in the eyes using an *in vivo* imaging system. The fluorescence signal in the CataKNexo group was sustained for 7 days, while it was sustained for only 5 days in the Nexo and CataNexo groups (Figure 3B). Accordingly, the mean half-life of CataKNexo was 59 h, which was longer than that of CAT, Nexo, and CataNexo (18, 37, and 39 h, respectively) (Figure S3A). These results indicated that CataKNexo was eliminated more slowly than the two types of exosomes lacking K_{10} (Nexo and CataNexo). Correspondingly, the intraocular retention time of CAT was extended to 168 h in the CataKNexo group, while this value was only 72 h for free CAT (Figures S3B and S3C).

To observe the distribution of the exosomes in the eye, we subsequently extracted the eyeballs and performed fluorescence imaging analysis of the Cy5-SE-labeled exosomes. As shown in Figure 3C, Nexo, CataNexo, and CataKNexo all showed an inclined distribution in the posterior segment of the eye. This might be attributed to the protein on the Nexo membrane, which somehow interacts with the retina. Pursuing this, we performed proteomic analysis of the retinas of RIRI model mice and compared the results with those of CataKNexo (Figure S3D). Among these ligand-receptor pairs, we found that both CXC chemokine

(J) Proteomic analysis of fresh and Lyo/Reh CataKNexo. The abundance of characteristic proteins associated with exosomes, NSC, chemokine receptor, neuroprotection, and CAT was analyzed.

(K) miRNA sequencing of fresh and Lyo/Reh CataKNexo. Representative miRNAs related to antioxidants, neuroprotection, and anti-apoptosis were analyzed. Data in (F), (G), and (H) are mean ± SD and were compared using one-way ANOVA (F, H). The experiments in (B), (D), (E), and (I) were independently repeated three times with similar results. See also Figure S2.

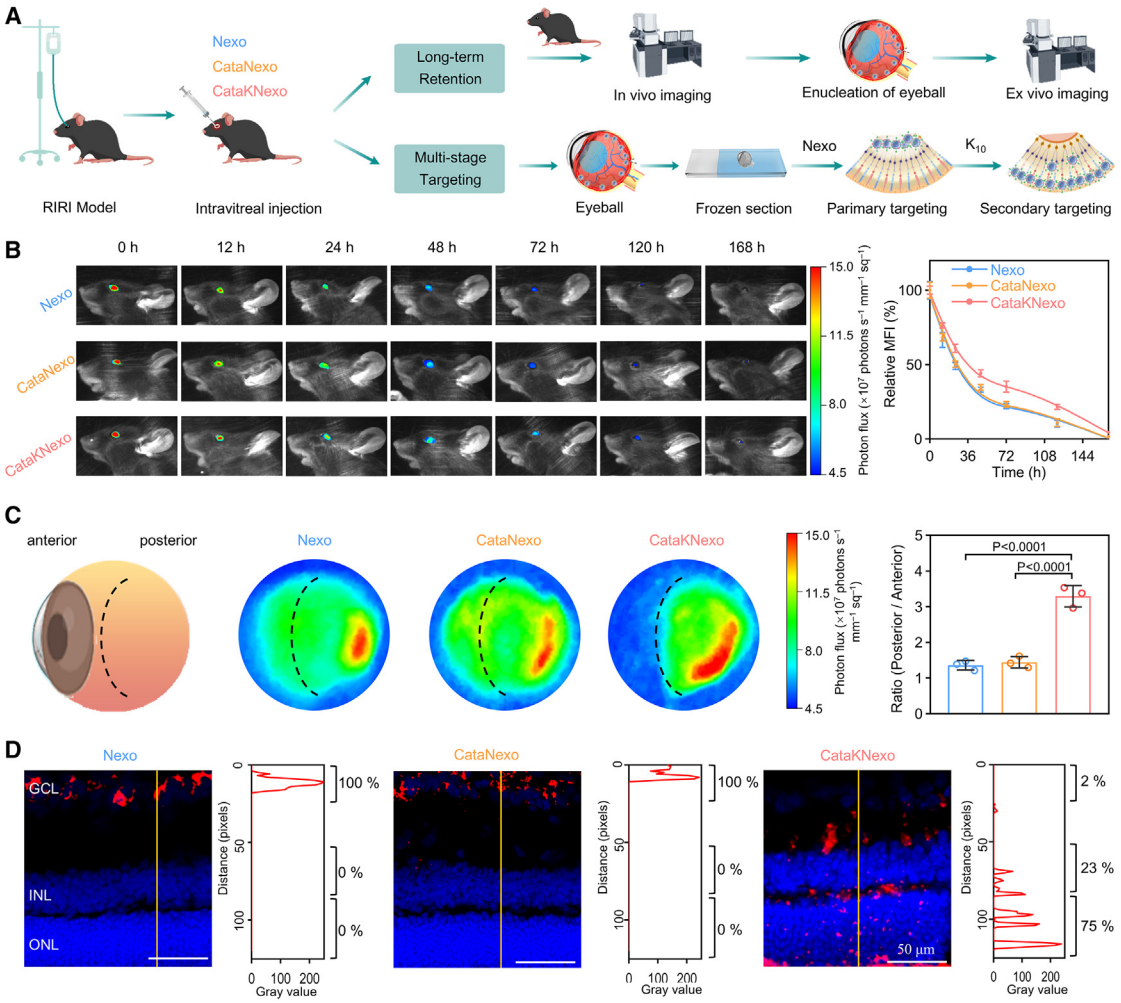

Figure 3. *In vivo* evaluation for the retention and multi-stage targeting of CataKNexo in RIRI model mice

(A) Schematic for evaluation of the intraocular retention and multi-stage targeting (Nexo, CataNexo, and CataKNexo) in RIRI model mice.

(B) Representative fluorescence images and quantitative analysis of the intraocular retention at the indicated time points after single intravitreal injection of Nexo, CataNexo, or CataKNexo (n = 3, 1 eye from each of 3 mice).

(C) Representative fluorescence images and quantitative analysis of excised eyeballs at 24 h after treated with various exosomes (n = 3, 1 eye from each of 3 mice, posterior: the right area of the dotted line represents the ocular structure behind the lens, anterior: the left area of the dotted line represents the ocular structure in front of the lens).

(D) Representative fluorescence images by CLSM and statistical analysis of the targeting in different groups (n = 3, 1 eye from each of 3 mice). Scale bar: 50 μm. The images are presented at the same magnification.

Data in (B) and (C) are mean ± SD and were compared using one-way ANOVA (C). The experiments in (B)–(D) were independently repeated three times with similar results. See also Figure S3.

receptor 4 (CXCR4) from CataKNexo and stromal cell-derived factor 1 (SDF1) from retina were in abundance, indicating the possibility of this pair participating in the retinal accumulation of CataKNexo. To verify this hypothesis, we conducted a blocking experiment, and as expected, blocking CXCR4 in CataKNexo (CataKNexo + anti-CXCR4) significantly compromised its accumulation in the retina (Figures S3E and S3F).

During the investigation of the intraocular distribution, we also observed another interesting phenomenon that CataKNexo was relatively more distributed in the posterior segment of the eye as compared to Nexo and CataNexo (Figure 3C). This could be attributed to the K_{10} component, which could guide more exosomes into deeper layers of the retina. To verify this unique penetration capacity, the retinas of the Nexo, CataNexo, and CataKNexo groups were sectioned with a freezing microtome and imaged using CLSM (Figure 3D). Neither Nexo nor CataNexo showed signs of penetration, while a large amount of CataKNexo was observed at the ONL, with the proportion jumping to 75%. Taken together, our results demonstrated that CataKNexo exhibited prolonged intraocular retention and multi-stage targeting.

Penetration of CataKNexo in an *in vitro* retinal model

Before evaluating the therapeutic efficacy, we were interested in how CataKNexo penetrated the ONL, which could gain a deeper

CellPress
OPEN ACCESS

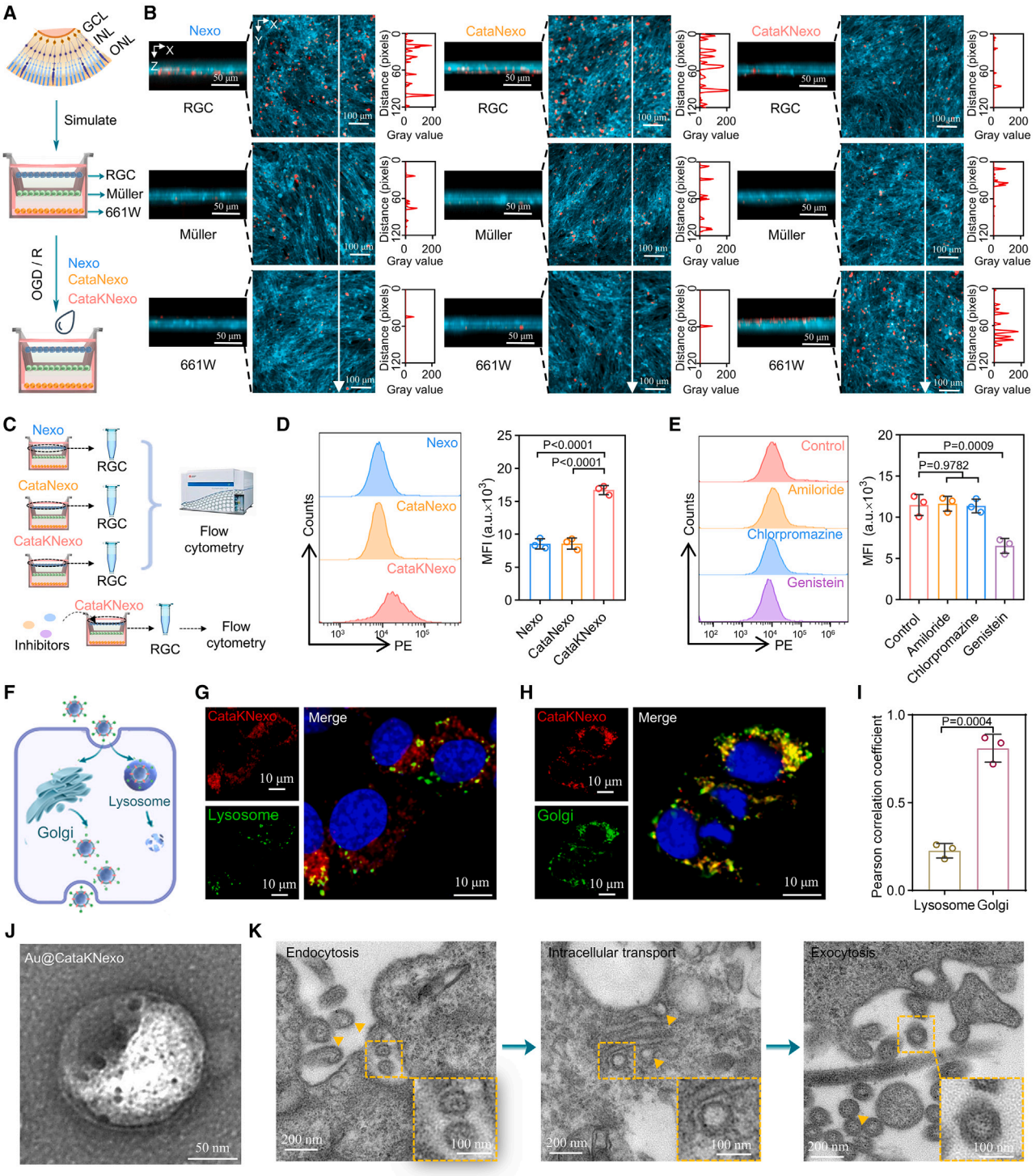

Figure 4. *In vitro* investigation of the penetration of CataKNexo into distinct cell layers of a simulated ocular structure

(A) Experimental design schematic for evaluating the penetration of CataKNexo using an *in vitro* model. In this iterative Transwell coculture system, retinal ganglion cells (RGCs, representing the GCL) were cultured in the top layer, Müller cells (representing the INL) were cultured in the middle layer, and 661W cells (representing the ONL) were cultured in the bottom layer.

(B) Representative CLSM images and analysis of the distribution after treatment with the indicated exosomes. The images of XZ (scale bar: 50 μm) and XY (scale bar: 100 μm) planes are presented with same magnification, respectively. Cyan: phalloidin-labeled cytoskeleton, red: PKH26-labeled exosomes.

(C) Experimental design schematic for the flow cytometry analysis.

(legend continued on next page)

understanding for precise targeting. In view of the challenges of employing animal models to probe exosome penetration, we attempted to establish an *in vitro* retinal model using an iterated Transwell apparatus. From top to bottom chambers, three layers of retinal ganglion cells (RGCs), Müller cells, and 661W cells were positioned to simulate the retina structure of RGCs, INL, and ONL, respectively (Figure 4A). The model apparatus was placed in an anaerobic incubator (5% CO_2 and 95% N_2) with glucose-free Dulbecco's modified Eagle's medium for 2 h, which was followed by exposure to a normoxic atmosphere with normal medium for 12 h. Such an oxygen-glucose deprivation/reperfusion (OGD/R) approach has been widely used for RVO.[40]

Following the aforementioned OGD/R injury, the top layer was exposed to PKH26-labeled Nexo, CataNexo, or CataKNexo for 24 h, demonstrating that CataKNexo had minimal effects on the cell phenotypes and activity of 661W cells (Figures S4A and S4B). As demonstrated by the CLSM images shown in Figure 4B, the CataKNexo signal was robust in 661W cells, whereas Nexo and CataNexo signals were predominantly observed in RGCs, supporting the important role of positive charges from the K_{10} modification in promoting their penetration into the layer representing the ONL (Figure 4B; Figure S4C). To determine the underlying mechanism, we studied the cellular endocytosis pathways and subsequent intracellular transport of CataKNexo in RGCs and Müller cells. After incubating Nexo, CataNexo, or CataKNexo with the Transwell apparatus for 4 h, we collected RGCs from the top layer for flow cytometry analysis (Figure 4C). Compared to Nexo and CataNexo, CataKNexo showed a significantly increased uptake by RGCs due to the positive charges from K_{10} conjugation (Figure 4D; Figure S4D). Further examining the cellular uptake of CataKNexo using inhibitors for distinct endocytosis pathways, we found a significantly inhibited uptake upon genistein pretreatment (Figure 4E; Figure S4D), indicating caveolae-mediated endocytosis as the primary endocytosis pathway.

After endocytosis, exosomes can be transported to lysosomes for degradation or to the Golgi apparatus for successive secretion (Figure 4F).[41] Accordingly, we performed CLSM imaging using LysoTracker Green or GolgiTracker Green probes to investigate CataKNexo localization. As displayed in Figures 4G–4I, only a few signals of internalized CataKNexo were colocalized with lysosomes (with a correlation coefficient [r] of 0.23), while most signals were colocalized with the Golgi apparatus (with a correlation coefficient [r] of 0.81). Moreover, we prepared Au@CataKNexo (Au nanoparticles labeled CataKNexo, Figure 4J) and added them to the *in vitro* retinal model, which enabled us to use TEM to observe the detailed process with a high resolution. As shown in Figure 4K, Au@CataKNexo were transported to the Golgi apparatus after endocytosis by RGCs and then secreted again. Similar transcytosis was also observed in Müller cells (Figures S4E–S4G), thus ensuring the arrival to the ONL (Figures S4H–S4K). Through further bioinformatics analysis (Figure S4L), we also found that the transcytosis function of 661W cells is weaker than Müller cells. This could explain the experimental phenomenon that CataKNexo penetrated the Müller cell layer while retained in the bottom layer of 661W cells, wherein the CataKNexo could exert the synergism of antioxidation and neuroprotection.

Therapeutic efficacy and safety of CataKNexo in RIRI model mice

The aforementioned results encouraged us to evaluate the therapeutic efficacy *in vivo*. Given that timely administration of medicine to prevent the death of retinal cells can effectively restore the function of the retina, we performed intravitreal administration of CataKNexo at 12 h after RIRI and observed the outcomes at 36 h after administration (Figure 5A). Genes associated with microglial activation,[42] such as *Trem2* and *Ctsz*, were also significantly downregulated following CataKNexo treatment (Figure S5A) and highlight the role of CataKNexo in promoting microglial homeostasis. To obtain a comprehensive understanding, we conducted transcriptome profiling of retinas from RIRI model mice after a single intravitreal injection of PBS or CataKNexo. Hierarchical clustering analysis of the differentially expressed genes revealed that CataKNexo significantly downregulated the genes associated with oxidative stress damage (e.g., *Rac2* and *Thbs1*), apoptosis (e.g., *Nlrc5* and *Irf9*), and inflammation (e.g., *TNF-*α and *IL-1*β), while upregulated the genes associated with photoreceptor cell function (e.g., *Rgr*, *Ttr*, and *Egr1*) (Figure 5B left). Gene set enrichment analysis revealed that CataKNexo particularly downregulated gene sets involved in H_2O_2-induced cell death, neuron death in response to oxidative

(D) Flow cytometry and corresponding quantitative analysis after endocytosis of Nexo, CataNexo, and CataKNexo in RGCs (n = 3 biologically independent experiments).
(E) Flow cytometry and corresponding quantitative analysis after endocytosis of CataKNexo in RGCs with the application of the indicated inhibitors for distinct endocytosis pathways (n = 3 biologically independent experiments). Amiloride is an inhibitor of macropinocytosis; chlorpromazine is an inhibitor of clathrin-mediated endocytosis; genistein is an inhibitor of caveolae-mediated endocytosis.
(F) Schematic for the anticipated transport of CataKNexo in RGCs.
(G) Representative CLSM fluorescence images showing co-localization of PKH26 with LysoTracker fluorescence in RGCs. Blue: DAPI, red: PKH26-labeled CataKNexo, green: LysoTracker-labeled lysosome. The images on the left (scale bar: 10 μm) are presented with same magnification.
(H) Representative CLSM fluorescence images showing colocalization of PKH26 with GolgiTracker fluorescence in RGCs. Blue: DAPI, red: PKH26-labeled CataKNexo, green: GolgiTracker-labeled Golgi apparatus. The images on the left (scale bar: 10 μm) are presented with same magnification.
(I) Corresponding Pearson correlation coefficients of PKH26 with LysoTracker Green or GolgiTracker Green fluorescence calculated by pixel intensity using ImageJ software (n = 3 biologically independent experiments).
(J) TEM image of Au nanoparticle-labeled CataKNexo stained with uranyl acetate. Scale bar: 50 nm.
(K) TEM images of endocytosis, intracellular transport, and exocytosis of Au nanoparticle-labeled CataKNexo in RGCs. The images (scale bar: 200 nm) and insets on the right (scale bar: 100 nm) are presented with same magnification, respectively.
Data in (D), (E), and (I) are mean ± SD and were compared using one-way ANOVA (D, E) or two-tailed unpaired Student's t test (I). The experiments in (B), (G), (H), (J), and (K) were independently repeated three times with similar results. See also Figure S4.

CellPress
OPEN ACCESS

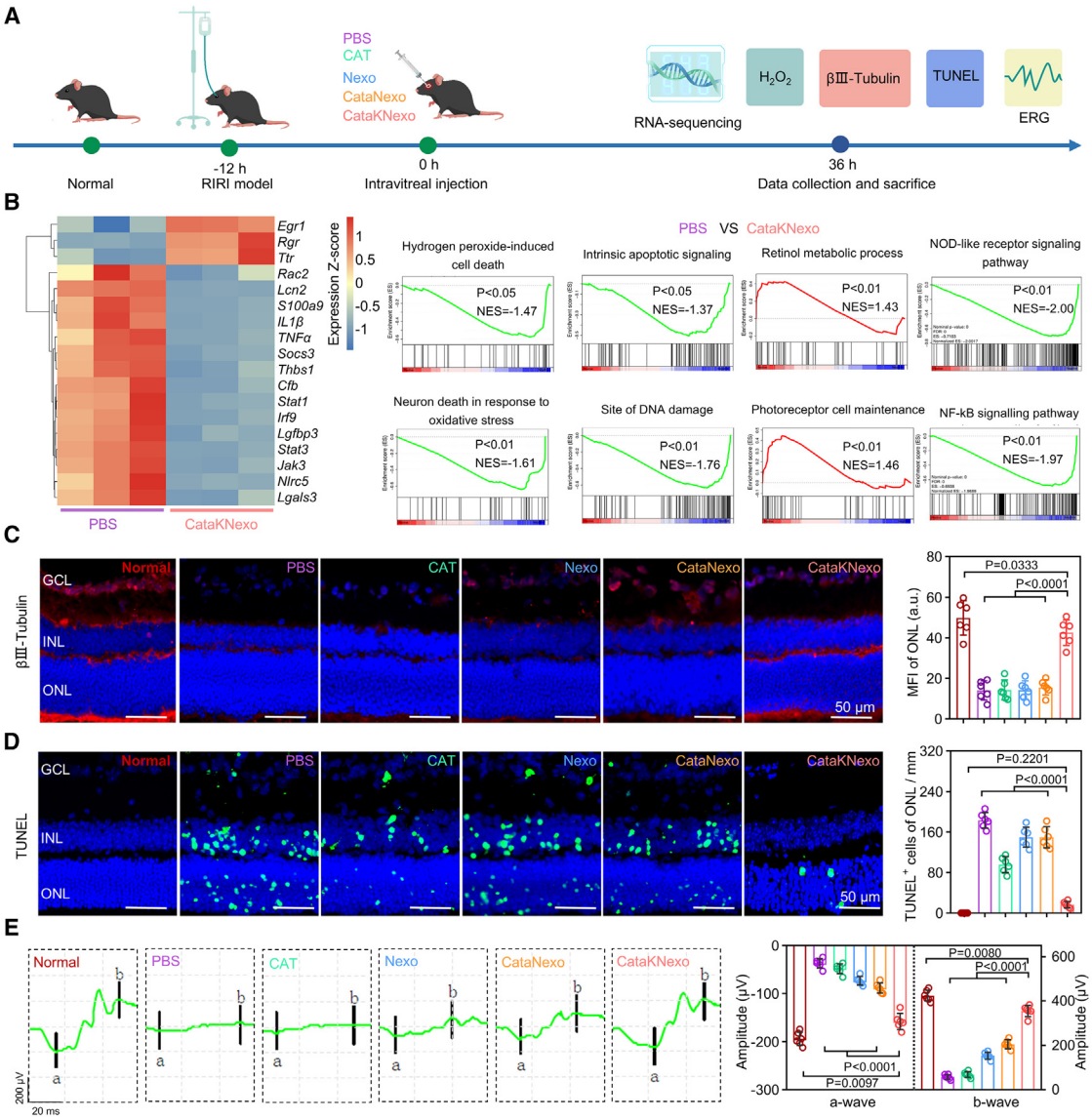

Figure 5. Therapeutic efficacy and safety of CataKNexo in RIRI model mice

(A) Schematic for evaluating the therapeutic benefit of CataKNexo for the treatment of RIRI model mice.

(B) Transcriptome analysis (left, n = 3, 1 eye from each of 3 mice) of retinas from RIRI mice after intravitreal injection with PBS or CataKNexo, and gene set enrichment analysis (GSEA) (right) of the PBS group versus the CataKNexo group.

(C) Representative neuroprotein fluorescent images obtained by CLSM and quantitative analysis of retinal sections from the various groups (n = 6, 1 eye from each of 6 mice). Scale bar: 50 μm. The images are presented at the same magnification.

(D) Representative CLSM images for cell damage and quantitative analysis of retinal sections in the indicated groups (n = 6, 1 eye from each of 6 mice). Scale bar: 50 μm. The images are presented at the same magnification.

(E) Representative ERG images presenting the retinal photoelectric conversion function and quantitative analysis of a-wave and b-wave amplitudes in the various groups (n = 6, 1 eye from each of 6 mice).

Data in (C)–(E) are mean ± SD and were compared using one-way ANOVA. The experiments in (C)–(E) were independently repeated three times with similar results. See also Figure S5.

stress, intrinsic apoptotic signaling, site of DNA damage and inflammation, as well as upregulated gene sets involved in retinol metabolic processes and photoreceptor cell maintenance (Figure 5B right). This finding highlights the role of CataKNexo in promoting microglial homeostasis. The aforementioned gene regulatory functions could be attributed to the therapeutic components of CataKNexo, as shown in Figures 2J and 2K. For instance, CAT is highly effective in scavenging H_2O_2, while neurotrophic nerve growth factor (NGF) and anti-inflammatory miRNA-122-5p from exosomes function in exerting neuroprotection, both of which may work together to substantially reduce retina apoptosis.[43,44]

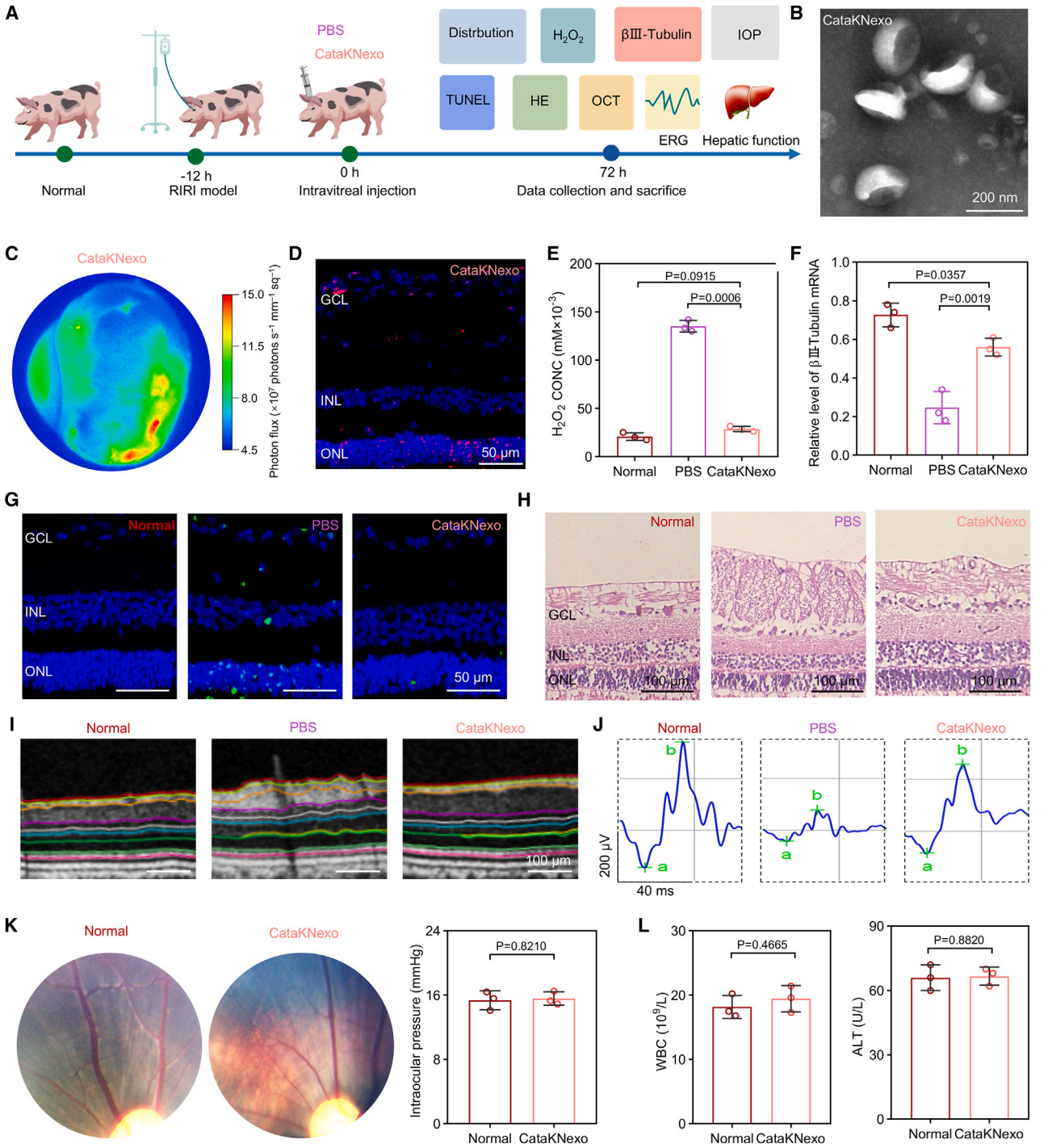

Figure 6. Distribution, therapeutic efficacy, and safety of CataKNexo in RIRI model Bama miniature pigs

(A) Schematic for evaluating the therapeutic benefit and safety of CataKNexo in a Bama miniature pig RIRI model. The exosomes are derived from human neural stem cells.

(B) TEM image of CataKNexo stained with uranyl acetate. Scale bar: 200 nm.

(C) Fluorescence image of excised eyeball at 72 h after single intravitreal injection of CataKNexo.

(D) Retinal section imaged using CLSM to evaluate the retinal penetration of CataKNexo. Scale bar: 50 μm.

(E) Measurement of H_2O_2 concentration using a H_2O_2 Content Assay Kit after treatment with PBS or CataKNexo (n = 3, 1 eye from each of 3 pigs).

(F) PCR analysis of retinal βIII-Tubulin in the PBS and CataKNexo groups (n = 3, 1 eye from each of 3 pigs).

(legend continued on next page)

Subsequently, we evaluated the potential therapeutic utility of CataKNexo in the RIRI model mice mentioned earlier. Model mice were divided into five groups, each receiving a single intravitreal injection of PBS, CAT, Nexo, CataNexo, and CataKNexo, separately. The measurement of H_2O_2 content showed that CataKNexo significantly reduced H_2O_2 levels compared to other groups, benefiting from the CAT scavenging (Figure S5B). Moreover, CataKNexo exhibited the most enhanced expression of βIII-Tubulin (a neuron-specific protein) in the ONL under the function of neuroprotective factors from the Nexo chassis (Figure 5C).[45,46] Additionally, retinal staining of terminal deoxynucleotidyl transferase dUTP nick-end labeling (TUNEL) revealed that the CataKNexo group had a significant reduction in the extent of apoptotic cells of ONL compared to the other groups (Figure 5D).

Shifting our attention to the whole retina, CataKNexo also resulted in the most reduced cell apoptosis compared to the other groups (Figures S5C and S5D), which promoted us to evaluate vision function (Figure 5E). The results demonstrated a significant reduction in the amplitude of both the a-wave and b-wave in the PBS group, with the electrophysiological curve appearing nearly flat. In contrast, other groups, including CAT, Nexo, and CataNexo, were able to alleviate the reduction in the amplitudes of both a-wave and b-wave. Notably, the CataKNexo group again outperformed other treatments, with a 4.3-fold increase in the a-wave and a 6.2-fold increase in the b-wave compared with the PBS group. Moreover, such a potent therapeutic efficacy of CataKNexo was also superior to the combination of two clinically used agents (neuroprotective NGF and antioxidative N-acetylcysteine, Figure S5E). In addition, we observed that CataNexo, with its ROS-scavenging function, offers superior tissue protection compared to Nexo alone, demonstrating the role of H_2O_2 clearance in mitigating tissue injury.[47] Overall, no side effects related to intraocular pressure, complete blood count, blood biochemistry, or the histological characteristics of the heart, liver, spleen, lung, or kidney were observed (Figures S5F and S5G), further supporting the safety of intravitreal administration of CataKNexo.

Therapeutic efficacy and safety of CataKNexo in RIRI model Bama miniature pigs

Finally, we aimed to assess the efficacy and safety of CataKNexo in a more clinically relevant RIRI pig model because the structure of the pig eye is more similar to that of the human eye than to that of mice. Six Bama miniature pigs weighing 12.5 ± 0.5 kg and aged 4 months were divided into two groups: the PBS group and the CataKNexo group. Considering the time scales of RIRI and therapeutic outcome, we administered CataKNexo at 12 h after retinal IR and observed the effect and safety at 72 h after administration (Figure 6A). The procedure for constructing CataKNexo applied in the RIRI pig model was the same as noted in Figure 2A, except that human NSCs were utilized for lentiviral transfection (Figure 6B; Figures S6A and S6B). To evaluate the targeting of CataKNexo, we first isolated eyeballs and assessed the fluorescence localization of exosomes. As shown in Figure 6C, CataKNexo was observed in the posterior segment of the eye, strongly suggesting the retinal accumulation of CataKNexo. We then conducted CLSM to scan retinal sections and again demonstrated that CataKNexo reached to the ONL (Figure 6D).

Inspired by the excellent multi-stage targeting of CataKNexo, we next evaluated its therapeutic utility in RIRI model pigs. In the CataKNexo group, the concentration of H_2O_2 in the vitreous humor exhibited a significant reduction compared to the PBS group (Figure 6E). On the other hand, polymerase chain reaction (PCR) results verified that CataKNexo treatment induced a 2.3-fold increase in retinal βIII-Tubulin mRNA levels in comparison to the PBS group (Figure 6F). Owing to the aforementioned two aspects, TUNEL staining of the retina showed that CataKNexo remarkably reduced the apoptosis of photoreceptor cells in the retinal ONL (Figure 6G; Figure S6C). Accordingly, hematoxylin and eosin (H&E) staining showed that CataKNexo increased the row numbers of retinal ONL by 1.7-fold (Figure 6H; Figure S6D). Given that the pig eye allows us to conduct optical coherence tomography (OCT), we also performed this invasive *in vivo* assessment (Figure 6I; Figure S6E). The PBS group exhibited retinal edema resulting from acute oxidative stress injury, whereas the retinal edema was significantly alleviated after intravitreal injection of CataKNexo. Consequently, electroretinogram (ERG) examination showed that the amplitudes of a-wave and b-wave in the CataKNexo group were significantly increased compared to the PBS group, indicating a satisfactory recovery of vision function (Figure 6J; Figure S6F). Consistent with the murine data, pigs receiving CataKNexo treatment had no obvious adverse effects on the vitreous body, retina, and intraocular pressure, as well as on hematological parameters and histological morphology of the heart, liver, spleen, lung, or kidney (Figures 6K and 6L; Figures S6G and S6H), again confirming the safety profile of this therapeutic.

(G) Representative TUNEL staining of retinal sections from the PBS and CataKNexo groups (n = 3, 1 eye from each of 3 pigs). Scale bar: 50 μm. The images are presented at the same magnification.
(H) Representative H&E staining of retinal sections in PBS and CataKNexo groups (n = 3, 1 eye from each of 3 pigs). Scale bar: 100 μm. The images are presented at the same magnification.
(I) Representative OCT images and quantitative analysis of ONL thickness in the PBS and CataKNexo groups (n = 3, 1 eye from each of 3 pigs). Scale bar: 100 μm. The images are presented at the same magnification.
(J) Representative images of full-field ERG and quantitative analysis of amplitudes of a-wave and b-wave in the PBS and CataKNexo groups (n = 3, 1 eye from each of 3 pigs).
(K) Color fundus photograph (left) and intraocular pressure (right) using an Icare TonoVet rebound tonometer for the assessment of local responses to the intravitreal injection of CataKNexo (n = 3, 1 eye from each of 3 pigs).
(L) Complete blood count (CBC, left) and blood biochemistry (right) for evaluation of side effects following intravitreal injection of CataKNexo (n = 3, 1 eye from each of 3 pigs).
Data in (E), (F), (K), and (L) are mean ± SD and were compared using one-way ANOVA (E, F) or two-tailed unpaired Student's t test (K, L). The experiments in (B)–(D) and (G)–(K) were independently repeated three times with similar results. See also Figure S6.

DISCUSSION

Through clinical data from the RVO cohort and experimental studies in mouse models of RIRI, we innovatively found that H_2O_2 is the main damage-causing ROS in RIRI and that the ONL is the region most susceptible to oxidative stress. This fundamental understanding derived from these investigations allows for the informed design of antioxidant materials, delineating the exact anatomical locations where their therapeutic intervention is most crucial for mitigating RIRI. We rationally engineered Nexo with dual modifications of CAT and K_{10} to construct our CataKNexo therapeutic. After intravitreal injection, we confirmed the multi-stage transport that accumulated at the retina and further penetrated into the ONL, wherein CataKNexo exerted synergistic antioxidant and neuroprotective effects. In both murine and porcine RIRI models, we ultimately observed potent therapeutic efficacy, with almost no side effects. In the future, we also need to study the response relationship between the severity of different fundus diseases, different time points of intervention, and dose, which can give us more guidance to better minimize the cost and improve the therapeutic efficacy.

Intravitreal injection is a commonly used and highly effective route of administration for treating retinal diseases.[48] However, the drug may diffuse in the vitreous cavity and act randomly on the retina after administration, which reduces its bioavailability.[49] In addition, drug molecules can be rapidly eliminated along with the aqueous humor circulation, resulting in a reduced effective concentration in the eye.[50] The limited retention period not only narrows the time window for diffusion to the retina in the posterior eye segment but also hinders effective targeting of the ONL. As the building chassis, the Nexo utilized in our study has particle sizes ranging from 50 to 200 nm, providing an extended retention period to facilitate accumulation within the retina. CataKNexo holds promise as a platform for precision therapy targeting ocular diseases. We anticipate that reducing the K_{10} density of CataKNexo can further target other layers of the retina, such as the INL, thus providing a precise strategy for treating macular edema and endophytic retinoblastoma.

Nexo exhibits robust phenotypic signatures and is abundant in chemokine receptors and neurotrophic factors, which make the system promising for targeting and repairing neurocyte damage.[51] In tandem with repairing damaged ocular tissues, mitigating oxidative stress represents a pivotal therapeutic axis to radically remedy RIRI. Traditional antioxidants (such as vitamin C, vitamin E, and glutathione) are expendable, and the dosage is limited owing to the capacity of the vitreous cavity, which is inadequate for treating severe tissue damage caused by intense oxidative stress. Although some synthetic nanomaterials possessing both catalytic properties (such as manganese oxide, cerium oxide, and vanadium carbide) have been developed, their clinical translation is limited by insufficient clinical studies.[52,53] In sharp contrast, antioxidant enzymes theoretically enable the repeated catalysis of substrates, achieving persistent antioxidant functionality and well-proven safety.[54] Considering that most natural enzymes are entirely encoded by genes, synthetic biology provides a straightforward and adaptable method to enable Nexo to express designated enzymes. This extends beyond CAT to include options such as SOD or GPX, depending solely on the specific requirements of different diseases.

In addition to altering the displayed components to modulate functionality, our therapeutic strategy can be synergistically combined with other interventions for the treatment of various retinal diseases. In the pathogenesis of diabetic retinopathy (DR), initial oxidative stress injury causes neovascularization, which further exacerbates the condition of patients.[55] Combining CataKNexo with an antivascular endothelial growth factor (e.g., ranibizumab) through synthetic biology can reduce oxidative stress damage and neovascularization, which may help prevent the exacerbation of proliferative changes of DR.[56] Additionally, inflammation may occur in the retinas of some patients with RVO; therefore, the loading of anti-inflammatory medications (e.g., dexamethasone) with CataKNexo may better reduce the retina edema and intraretinal infiltration of inflammatory cells and hereby restore the retinal function of patients with RVO.[57,58]

Limitations of the study

The limitations of our study include the use of mouse and human NSC lines, where primary NSCs exhibit phenotypic instability after gene transfection, posing a challenge for exosome extraction. To facilitate clinical translation, we consider mesenchymal stem cells as the alternative targets of gene transfection in the future. In addition, more efforts should be made on their stability and mass production.[59] Our results showed that CataKNexo exhibited good stability with little change in size and zeta potential after 3 weeks of storage in the refrigerator or after freeze-drying and thawing. In the future, additional measures, such as the incorporation of freeze-drying protectants, could be explored to further enhance its storage stability. For yield optimization, one strategy involves converting 2D cultures into 3D cultures, which can enhance parent cell density and increase exosome yield.[60] Additionally, efficient exosome production can be facilitated by adjusting the culture medium (i.e., glucose starvation, acidic pH, and shear stress)[18] or by co-expressing activator genes (i.e., HSP20, TSPAN6, and CD9)[61] of exosome biogenesis. Note that it is crucial to ensure that these interventions do not induce any undesired alterations in stem cell phenotypes.

RESOURCE AVAILABILITY

Lead contact

Further information and requests for resources and reagents should be directed to and will be fulfilled by the lead contact, Yong Tao (taoyong@mail.ccmu.edu.cn).

Materials availability

All unique/stable reagents generated in this study are available from the lead contact with a completed materials transfer agreement.

Data and code availability

- miRNA-seq and RNA-seq data have been deposited at NCBI BioProject (accession number: PRJNA1056442) and are publicly available as of the date of publication.
- The proteomics data have been deposited at the ProteomeXchange Consortium via the iProX partner repository (PXD048582) and are publicly available as of the date of publication.

- This study does not report original code.
- Any additional information required to reanalyze the data reported in this paper is available from the lead contact upon request.

ACKNOWLEDGMENTS

This work was supported by the National Natural Science Foundation of China (T2225021 to W.W., 82471081 to Y.T., 21821005 to G.M., and 52203185 to D.Z.), the CAS Project for Young Scientists in Basic Research (YSBR-083 to W.W.), the Beijing Natural Science Foundation (JQ21027 to W.W.), the Beijing Hospitals Authority's Ascent Programme (DFL20220301 to Y.T.), the Beijing Nova Program (20230484445 to Y.T. and W.W.), the Capital Health Development Scientific Research Project Grant (SF 2022-2-2035 to Y.T.), the Excellent Young Talent Innovation Project of Chinese Institutes for Medical Research (CX23YQA02 to Y.T.), the Chinese Institutes for Medical Research (CX23YQ03 to Y.T.), the Golden Seed Fund Project of Beijing Chaoyang Hospital (CYJZ202139 to X.W.), and the Youth Project of Beijing Hospital Management Center (QML20211703 to W.K.).

AUTHOR CONTRIBUTIONS

W.W., Y.T., and G.M. conceived and designed the study. W.Y. and X.W. performed most of the experiments and analyzed the data. J.F., X.W., and W.K. collected and analyzed the clinical samples. Y.L. assisted with the cell experiments. D.Z. provided suggestions about the data presentation. W.W., X.W., and W.Y. wrote the original draft manuscript. W.W., Y.T., G.M., X.W., and D.Z. revised the manuscript. All authors reviewed the manuscript and approved the final version.

DECLARATION OF INTERESTS

The authors declare no competing interests.

STAR★METHODS

Detailed methods are provided in the online version of this paper and include the following:

SUPPLEMENTAL INFORMATION

Supplemental information can be found online at https://doi.org/10.1016/j.xcrm.2025.102052.

Received: July 3, 2024
Revised: October 15, 2024
Accepted: March 10, 2025
Published: April 15, 2025

REFERENCES

1. Wong, T.Y., and Scott, I.U. (2010). Retinal-Vein Occlusion. N. Engl. J. Med. *363*, 2135–2144. https://doi.org/10.1056/NEJMcp1003934.
2. Li, Y., Hall, N.E., Pershing, S., Hyman, L., Haller, J.A., Lee, A.Y., Lee, C.S., Chiang, M., Lum, F., Miller, J.W., et al. (2022). Age, Gender, and Laterality of Retinal Vascular Occlusion: A Retrospective Study from the IRIS Registry. Ophthalmol. Retina *6*, 161–171. https://doi.org/10.1016/j.oret.2021.05.004.
3. Stitt, A.W., O'Neill, C.L., O'Doherty, M.T., Archer, D.B., Gardiner, T.A., and Medina, R.J. (2011). Vascular stem cells and ischaemic retinopathies. Prog. Retin. Eye Res. *30*, 149–166. https://doi.org/10.1016/j.preteyeres.2011.02.001.
4. Ting, D.S.W., Cheung, G.C.M., and Wong, T.Y. (2016). Diabetic retinopathy: global prevalence, major risk factors, screening practices and public health challenges: a review. Clin. Exp. Ophthalmol. *44*, 260–277. https://doi.org/10.1111/ceo.12696.
5. Jayaram, H., Kolko, M., Friedman, D.S., and Gazzard, G. (2023). Glaucoma: now and beyond. Lancet *402*, 1788–1801. https://doi.org/10.1016/s0140-6736(23)01289-8.
6. Zhang, Z., Peng, S., Xu, T., Liu, J., Zhao, L., Xu, H., Zhang, W., Zhu, Y., and Yang, Z. (2023). Retinal Microenvironment-Protected Rhein-GFFYE Nanofibers Attenuate Retinal Ischemia-Reperfusion Injury via Inhibiting Oxidative Stress and Regulating Microglial/Macrophage M1/M2 Polarization. Adv. Sci. *10*, e2302909. https://doi.org/10.1002/advs.202302909.
7. Zhou, X., Lv, J., Li, G., Qian, T., Jiang, H., Xu, J., Cheng, Y., and Hong, J. (2021). Rescue the retina after the ischemic injury by polymer-mediated intracellular superoxide dismutase delivery. Biomaterials *268*, 120600. https://doi.org/10.1016/j.biomaterials.2020.120600.
8. Chew, E.Y. (2009). Laser photocoagulation and intravitreal injection of triamcinolone for retinal vein occlusions. JAMA *302*, 1693–1695. https://doi.org/10.1001/jama.2009.1523.
9. Hayreh, S.S. (2021). Photocoagulation for retinal vein occlusion. Prog. Retin. Eye Res. *85*, 100964. https://doi.org/10.1016/j.preteyeres.2021.100964.
10. Savitz, S.I., Yavagal, D., Rappard, G., Likosky, W., Rutledge, N., Graffagnino, C., Alderazi, Y., Elder, J.A., Chen, P.R., Budzik, R.F., Jr., et al. (2019). A Phase 2 Randomized, Sham-Controlled Trial of Internal Carotid Artery Infusion of Autologous Bone Marrow-Derived ALD-401 Cells in Patients With Recent Stable Ischemic Stroke (RECOVER-Stroke). Circulation *139*, 192–205. https://doi.org/10.1161/circulationaha.117.030659.
11. Jiang, X.C., Xiang, J.J., Wu, H.H., Zhang, T.Y., Zhang, D.P., Xu, Q.H., Huang, X.L., Kong, X.L., Sun, J.H., Hu, Y.L., et al. (2019). Neural Stem Cells Transfected with Reactive Oxygen Species-Responsive Polyplexes for Effective Treatment of Ischemic Stroke. Adv. Mater. *31*, e1807591. https://doi.org/10.1002/Adma.201807591.
12. Traverse, J.H., Henry, T.D., Pepine, C.J., Willerson, J.T., and Ellis, S.G. (2014). One-year follow-up of intracoronary stem cell delivery on left

ventricular function following ST-elevation myocardial infarction. JAMA *311*, 301–302. https://doi.org/10.1001/jama.2013.282674.

13. Zhang, K., and Cheng, K. (2023). Stem cell-derived exosome versus stem cell therapy. Nat. Rev. Bioeng. *1*, 608–609. https://doi.org/10.1038/s44222-023-00064-2.

14. Stern, J.H., Tian, Y., Funderburgh, J., Pellegrini, G., Zhang, K., Goldberg, J.L., Ali, R.R., Young, M., Xie, Y., and Temple, S. (2018). Regenerating Eye Tissues to Preserve and Restore Vision. Cell Stem Cell *23*, 453. https://doi.org/10.1016/j.stem.2018.08.014.

15. Shan, L., Xu, G., Yao, R.W., Luan, P.F., Huang, Y., Zhang, P.H., Pan, Y.H., Zhang, L., Gao, X., Li, Y., et al. (2023). Nucleolar URB1 ensures 3' ETS rRNA removal to prevent exosome surveillance. Nature *615*, 526–534. https://doi.org/10.1038/s41586-023-05767-5.

16. Kalluri, R., and McAndrews, K.M. (2023). The role of extracellular vesicles in cancer. Cell *186*, 1610–1626. https://doi.org/10.1016/j.cell.2023.03.010.

17. Wang, Z., Popowski, K.D., Zhu, D., de Juan Abad, B.L., Wang, X., Liu, M., Lutz, H., De Naeyer, N., DeMarco, C.T., Denny, T.N., et al. (2022). Exosomes decorated with a recombinant SARS-CoV-2 receptor-binding domain as an inhalable COVID-19 vaccine. Nat. Biomed. Eng. *6*, 791–805. https://doi.org/10.1038/s41551-022-00902-5.

18. Yang, Z., Shi, J., Xie, J., Wang, Y., Sun, J., Liu, T., Zhao, Y., Zhao, X., Wang, X., Ma, Y., et al. (2020). Large-scale generation of functional mRNA-encapsulating exosomes via cellular nanoporation. Nat. Biomed. Eng. *4*, 69–83. https://doi.org/10.1038/s41551-019-0485-1.

19. Stoll, G., and Nieswandt, B. (2019). Thrombo-inflammation in acute ischaemic stroke - implications for treatment. Nat. Rev. Neurol. *15*, 473–481. https://doi.org/10.1038/s41582-019-0221-1.

20. Fan, L., Liu, C., Chen, X., Zheng, L., Zou, Y., Wen, H., Guan, P., Lu, F., Luo, Y., Tan, G., et al. (2022). Exosomes-Loaded Electroconductive Hydrogel Synergistically Promotes Tissue Repair after Spinal Cord Injury via Immunoregulation and Enhancement of Myelinated Axon Growth. Adv. Sci. *9*, e2105586. https://doi.org/10.1002/Advs.202105586.

21. Zhang, Y., Kim, M.S., Jia, B., Yan, J., Zuniga-Hertz, J.P., Han, C., and Cai, D. (2017). Hypothalamic stem cells control ageing speed partly through exosomal miRNAs. Nature *548*, 52–57. https://doi.org/10.1038/nature23282.

22. Bian, B., Zhao, C., He, X., Gong, Y., Ren, C., Ge, L., Zeng, Y., Li, Q., Chen, M., Weng, C., et al. (2020). Exosomes derived from neural progenitor cells preserve photoreceptors during retinal degeneration by inactivating microglia. J. Extracell. Vesicles *9*, 1748931. https://doi.org/10.1080/20013078.2020.1748931.

23. Iyaswamy, A., Thakur, A., Guan, X.J., Krishnamoorthi, S., Fung, T.Y., Lu, K., Gaurav, I., Yang, Z., Su, C.F., Lau, K.F., et al. (2023). Fe65-engineered neuronal exosomes encapsulating corynoxine-B ameliorate cognition and pathology of Alzheimer's disease. Signal Transduct. Target. Ther. *8*, 404. https://doi.org/10.1038/s41392-023-01657-4.

24. Kong, W., Li, X., Guo, X., Sun, Y., Chai, W., Chang, Y., Huang, Q., Wang, P., and Wang, X. (2024). Ultrasound-Assisted CRISPRi-Exosome for Epigenetic Modification of α-Synuclein Gene in a Mouse Model of Parkinson's Disease. ACS Nano *18*, 7837–7851. https://doi.org/10.1021/acsnano.3c05864.

25. Qin, T., Li, C., Xu, Y., Qin, Y., Jin, Y., He, R., Luo, Z., Zhao, J., Duan, C., Lu, H., et al. (2024). Local delivery of EGFR+NSCs-derived exosomes promotes neural regeneration post spinal cord injury via miR-34a-5p/HDAC6 pathway. Bioact. Mater. *33*, 424–443. https://doi.org/10.1016/j.bioactmat.2023.11.013.

26. Wu, T., Liu, Y., Cao, Y., and Liu, Z. (2022). Engineering Macrophage Exosome Disguised Biodegradable Nanoplatform for Enhanced Sonodynamic Therapy of Glioblastoma. Adv. Mater. *34*, e2110364. https://doi.org/10.1002/Adma.202110364.

27. Huang, P., Feng, L., Oldham, E.A., Keating, M.J., and Plunkett, W. (2000). Superoxide dismutase as a target for the selective killing of cancer cells. Nature *407*, 390–395. https://doi.org/10.1038/35030140.

28. Mason, R.P., Casu, M., Butler, N., Breda, C., Campesan, S., Clapp, J., Green, E.W., Dhulkhed, D., Kyriacou, C.P., and Giorgini, F. (2013). Glutathione peroxidase activity is neuroprotective in models of Huntington's disease. Nat. Genet. *45*, 1249–1254. https://doi.org/10.1038/ng.2732.

29. Cowan, C.S., Renner, M., De Gennaro, M., Gross-Scherf, B., Goldblum, D., Hou, Y., Munz, M., Rodrigues, T.M., Krol, J., Szikra, T., et al. (2020). Cell Types of the Human Retina and Its Organoids at Single-Cell Resolution. Cell *182*, 1623–1640.e34. https://doi.org/10.1016/j.cell.2020.08.013.

30. Masland, R.H. (2001). The fundamental plan of the retina. Nat. Neurosci. *4*, 877–886. https://doi.org/10.1038/nn0901-877.

31. Khayat, M., Perais, J., Wright, D.M., Williams, M., and Lois, N. (2021). Anatomic-Functional Correlates in Lesions of Retinal Vein Occlusion. Investig. Ophthalmol. Vis. Sci. *62*, 10. https://doi.org/10.1167/iovs.62.7.10.

32. Kingston, B.R., Lin, Z.P., Ouyang, B., MacMillan, P., Ngai, J., Syed, A.M., Sindhwani, S., and Chan, W.C.W. (2021). Specific Endothelial Cells Govern Nanoparticle Entry into Solid Tumors. ACS Nano *15*, 14080–14094. https://doi.org/10.1021/acsnano.1c04510.

33. Zhou, Q., Shao, S., Wang, J., Xu, C., Xiang, J., Piao, Y., Zhou, Z., Yu, Q., Tang, J., Liu, X., et al. (2019). Enzyme-activatable polymer-drug conjugate augments tumour penetration and treatment efficacy. Nat. Nanotechnol. *14*, 799–809. https://doi.org/10.1038/s41565-019-0485-z.

34. Hwang, D.K., Chang, Y.L., Lin, T.C., Peng, C.H., Chien, K.H., Tsai, C.Y., Chen, S.J., Chen, K.H., and Hsu, M.Y. (2020). Changes in the Systemic Expression of Sirtuin-1 and Oxidative Stress after Intravitreal Anti-Vascular Endothelial Growth Factor in Patients with Retinal Vein Occlusion. Biomolecules *10*, 1414. https://doi.org/10.3390/biom10101414.

35. Chen, K.H., Hsiang, E.L., Hsu, M.Y., Chou, Y.C., Lin, T.C., Chang, Y.L., Tsai, C.Y., Li, T.H., Woung, L.C., Chen, S.J., et al. (2019). Elevation of serum oxidative stress in patients with retina vein occlusions. Acta Ophthalmol. *97*, 290–295. https://doi.org/10.1111/aos.13892.

36. Agardh, C.D., Gustavsson, C., Hagert, P., Nilsson, M., and Agardh, E. (2006). Expression of antioxidant enzymes in rat retinal ischemia followed by reperfusion. Metabolism *55*, 892–898. https://doi.org/10.1016/j.metabol.2006.02.016.

37. Chen, B., Caballero, S., Seo, S., Grant, M.B., and Lewin, A.S. (2009). Delivery of antioxidant enzyme genes to protect against ischemia/reperfusion-induced injury to retinal microvasculature. Invest. Ophth. Vis. Sci. *50*, 5587–5595. https://doi.org/10.1167/iovs.09-3633.

38. Ho, K.L., Yong, P.H., Wang, C.W., Lim, S.H., Kuppusamy, U.R., Arumugam, B., Ngo, C.T., and Ng, Z.X. (2024). *In vitro* anti-inflammatory activity and molecular docking of Peperomia pellucida (L.) Kunth extract via the NF-κB and PPAR-γ signalling in human retinal pigment epithelial cells. Bioorg. Chem. *153*, 107969. https://doi.org/10.1016/j.bioorg.2024.107969.

39. Scharf, J., Freund, K.B., Sadda, S., and Sarraf, D. (2021). Paracentral acute middle maculopathy and the organization of the retinal capillary plexuses. Prog. Retin. Eye Res. *81*, 100884. https://doi.org/10.1016/j.preteyeres.2020.100884.

40. Lai, Y., Lin, P., Chen, M., Zhang, Y., Chen, J., Zheng, M., Liu, J., Du, H., Chen, R., Pan, X., et al. (2020). Restoration of L-OPA1 alleviates acute ischemic stroke injury in rats via inhibiting neuronal apoptosis and preserving mitochondrial function. Redox Biol. *34*, 101503. https://doi.org/10.1016/j.redox.2020.101503.

41. Sun, Q., Zhou, Z., Qiu, N., and Shen, Y. (2017). Rational Design of Cancer Nanomedicine: Nanoproperty Integration and Synchronization. Adv. Mater. *29*, e1606628. https://doi.org/10.1002/Adma.201606628.

42. Absinta, M., Maric, D., Gharagozloo, M., Garton, T., Smith, M.D., Jin, J., Fitzgerald, K.C., Song, A., Liu, P., Lin, J.P., et al. (2021). A lymphocyte-microglia-astrocyte axis in chronic active multiple sclerosis. Nature *597*, 709–714. https://doi.org/10.1038/s41586-021-03892-7.

43. Qi, D., Deng, W., Chen, X., Fan, S., Peng, J., Tang, X., Wang, D., Yu, Q., and Song, L. (2022). Adipose-Derived Circulating Exosomes Promote Protection of the Pulmonary Endothelial Barrier by Inhibiting EndMT and Oxidative Stress through Down-Regulation of the TGF-β Pathway: A Potential Explanation for the Obesity Paradox in ARDS. Oxid. Med. Cell. Longev. *2022*, 5475832. https://doi.org/10.1155/2022/5475832.

44. Tanaka, T., Okuda, H., Isonishi, A., Terada, Y., Kitabatake, M., Shinjo, T., Nishimura, K., Takemura, S., Furue, H., Ito, T., et al. (2023). Dermal macrophages set pain sensitivity by modulating the amount of tissue NGF through an SNX25-Nrf2 pathway. Nat. Immunol. *24*, 439–451. https://doi.org/10.1038/s41590-022-01418-5.

45. Geisert, E.E., and Frankfurter, A. (1989). The neuronal response to injury as visualized by immunostaining of class III beta-tubulin in the rat. Neurosci. Lett. *102*, 137–141. https://doi.org/10.1016/0304-3940(89)90068-2.

46. Zalis, M.C., Johansson, S., and Englund-Johansson, U. (2017). Immunocytochemical Profiling of Cultured Mouse Primary Retinal Cells. J. Histochem. Cytochem. *65*, 223–239. https://doi.org/10.1369/0022155416689675.

47. Weng, Q., Sun, H., Fang, C., Xia, F., Liao, H., Lee, J., Wang, J., Xie, A., Ren, J., Guo, X., et al. (2021). Catalytic activity tunable ceria nanoparticles prevent chemotherapy-induced acute kidney injury without interference with chemotherapeutics. Nat. Commun. *12*, 1436. https://doi.org/10.1038/s41467-021-21714-2.

48. Fagan, X.J., and Al-Qureshi, S. (2013). Intravitreal injections: a review of the evidence for best practice. Clin. Exp. Ophthalmol. *41*, 500–507. https://doi.org/10.1111/ceo.12026.

49. Huang, X., and Chau, Y. (2019). Intravitreal nanoparticles for retinal delivery. Drug Discov. Today *24*, 1510–1523. https://doi.org/10.1016/j.drudis.2019.05.005.

50. Del Amo, E.M., Rimpelä, A.K., Heikkinen, E., Kari, O.K., Ramsay, E., Lajunen, T., Schmitt, M., Pelkonen, L., Bhattacharya, M., Richardson, D., et al. (2017). Pharmacokinetic aspects of retinal drug delivery. Prog. Retin. Eye Res. *57*, 134–185. https://doi.org/10.1016/j.preteyeres.2016.12.001.

51. Vogel, A.D., Upadhya, R., and Shetty, A.K. (2018). Neural stem cell derived extracellular vesicles: Attributes and prospects for treating neurodegenerative disorders. EBioMedicine *38*, 273–282. https://doi.org/10.1016/j.ebiom.2018.11.026.

52. Huang, G., Zang, J., He, L., Zhu, H., Huang, J., Yuan, Z., Chen, T., and Xu, A. (2022). Bioactive Nanoenzyme Reverses Oxidative Damage and Endoplasmic Reticulum Stress in Neurons under Ischemic Stroke. ACS Nano *16*, 431–452. https://doi.org/10.1021/acsnano.1c07205.

53. He, L., Huang, G., Liu, H., Sang, C., Liu, X., and Chen, T. (2020). Highly bioactive zeolitic imidazolate framework-8-capped nanotherapeutics for efficient reversal of reperfusion-induced injury in ischemic stroke. Sci. Adv. *6*, eaay9751. https://doi.org/10.1126/sciadv.aay9751.

54. Yan, R., Ren, J., Wen, J., Cao, Z., Wu, D., Qin, M., Xu, D., Castillo, R., Li, F., Wang, F., et al. (2022). Enzyme Therapeutic for Ischemia and Reperfusion Injury in Organ Transplantation. Adv. Mater. *34*, e2105670. https://doi.org/10.1002/adma.202105670.

55. Kowluru, R.A., Kowluru, A., Mishra, M., and Kumar, B. (2015). Oxidative stress and epigenetic modifications in the pathogenesis of diabetic retinopathy. Prog. Retin. Eye Res. *48*, 40–61. https://doi.org/10.1016/j.preteyeres.2015.05.001.

56. Sun, J.K., Wang, P.W., Taylor, S., and Haskova, Z. (2019). Durability of Diabetic Retinopathy Improvement with As-Needed Ranibizumab: Open-Label Extension of RIDE and RISE Studies. Ophthalmology *126*, 712–720. https://doi.org/10.1016/j.ophtha.2018.10.041.

57. Nicholson, L., Talks, S.J., Amoaku, W., Talks, K., and Sivaprasad, S. (2022). Retinal vein occlusion (RVO) guideline: executive summary. Eye *36*, 909–912. https://doi.org/10.1038/s41433-022-02007-4.

58. Jovanovic, J., Liu, X., Kokona, D., Zinkernagel, M.S., and Ebneter, A. (2020). Inhibition of inflammatory cells delays retinal degeneration in experimental retinal vein occlusion in mice. Glia *68*, 574–588. https://doi.org/10.1002/glia.23739.

59. Cheng, K., and Kalluri, R. (2023). Guidelines for clinical translation and commercialization of extracellular vesicles and exosomes based therapeutics. Extracell. Vesicle *2*, 100029. https://doi.org/10.1016/j.vesic.2023.100029.

60. Lei, Y., and Schaffer, D.V. (2013). A fully defined and scalable 3D culture system for human pluripotent stem cell expansion and differentiation. Proc. Nat. Acad. Sci. *110*, 5039–5048. https://doi.org/10.1073/pnas.1309408110.

61. Jafari, D., Malih, S., Eini, M., Jafari, R., Gholipourmalekabadi, M., Sadeghizadeh, M., and Samadikuchaksaraei, A. (2020). Improvement, scaling-up, and downstream analysis of exosome production. Crit. Rev. Biotechnol. *40*, 1098–1112. https://doi.org/10.1080/07388551.2020.1805406.

62. Cederlund, M., Ghosh, F., Arnér, K., Andréasson, S., and Akerström, B. (2013). Vitreous levels of oxidative stress biomarkers and the radical-scavenger α1-microglobulin/A1M in human rhegmatogenous retinal detachment. Graefes Arch. Clin. Exp. Ophthalmol. *251*, 725–732. https://doi.org/10.1007/s00417-012-2113-6.

63. Hayreh, S.S., Klugman, M.R., Beri, M., Kimura, A.E., and Podhajsky, P. (1990). Differentiation of ischemic from non-ischemic central retinal vein occlusion during the early acute phase. Graefes Arch. Clin. Exp. Ophthalmol. *228*, 201–217. https://doi.org/10.1007/bf00920022.

64. Benchorin, G., Calton, M.A., Beaulieu, M.O., and Vollrath, D. (2017). Assessment of Murine Retinal Function by Electroretinography. Bio. Protoc. *7*, 2218. https://doi.org/10.21769/BioProtoc.2218.

STAR★METHODS

KEY RESOURCES TABLE

REAGENT or RESOURCE	SOURCE	IDENTIFIER
Antibodies		
Anti-ALIX antibody	Abcam	Cat# ab275377; RRID: AB_3644262
Anti-CD63 antibody	Abcam	Cat# ab315108; RRID: AB_3099512
Anti-TSG101 antibody	Abcam	Cat# ab125011; RRID:AB_10974262
Anti-SOX2 antibody	Abcam	Cat# ab92494; RRID:AB_10585428
Anti-Nestin antibody	Abcam	Cat# ab221660; RRID:AB_2909415
Anti-Opn1mW antibody	Abcam	Cat# ab236916; RRID: AB_3677258
Anti-γ-synuclein antibody	Abcam	Cat# ab315442; RRID: AB_3677259
Anti-CAT antibody	Abcam	Cat# ab209211; RRID:AB_3086611
Anti-β actin antibody	Abcam	Cat# ab115777; RRID:AB_10899528
Anti-SDF1 antibody	Abcam	Cat# ab25117; RRID:AB_2088164
Anti-βIII-Tubulin antibody	Abcam	Cat# ab18207; RRID:AB_444319
Anti-CXCR4 antibody	Abcam	Cat# ab181020; RRID:AB_2910168
Anti-Rabbit IgG H&L (Cy3)	Abcam	Cat# ab97075; RRID:AB_10679955
Anti-Goat Anti-Mouse IgG H&L (Cy3)	Abcam	Cat# ab97035; RRID:AB_10680176
Anti-Goat Anti-Rabbit IgG H&L (HRP)	Abcam	Cat# ab205718; RRID:AB_2819160
Biological samples		
Vitreous humor in patients with idiopathic macular epiretinal membrane/idiopathic macular hole	Beijing Chaoyang Hospital	N/A
Vitreous humor in patients with RVO	Beijing Chaoyang Hospital	N/A
Chemicals, peptides, and recombinant proteins		
3, 3′-dioctadecyloxacarbocyanine perchlorate (DiO)	Beyotime Biotechnology.	Cat# C1038
Lysine polypeptide	Sangon Biotech	N/A
Fluorescein isothiocyanate	Solarbio Life Sciences	Cat# F8070
PKH26	Solarbio Life Sciences	Cat# D0030
Cyanine5 NHS ester	Solarbio Life Sciences	Cat# IC0790
FITC-Phalloidin	Solarbio Life Sciences	Cat# CA1620
4′, 6-diamidino-2-phenylindole	Solarbio Life Sciences	Cat# C0065
NGF	Solarbio Life Sciences	Cat# P00114
Amiloride	MedChemEpress	Cat# HY-B0285
Chlorpromazine	MedChemEpress	Cat# HY-12708
Genistein	MedChemEpress	Cat# HY-14596
Golgi-Tracker Green	Beyotime Biotechnology	Cat# C1045S
Lyso-Tracker Green	Beyotime Biotechnology	Cat# C1047S
NAC	Beyotime Biotechnology	Cat# S0077
Fetal bovine serum	Gibco	Cat# A5670701
Dulbecco's modified Eagle's medium	Gibco	Cat# 11965092
Penicillin-streptomycin	Sigma-Aldrich	Cat# P4458
Catalase	Sigma-Aldrich	Cat# 60634
Critical commercial assays		
Micro SOD Activity Assay Kits	Solarbio Life Sciences	Cat# BC5165
CAT Activity Assay Kits	Solarbio Life Sciences	Cat# BC0205
GPX Activity Assay Kits	Solarbio Life Sciences	Cat# BC1190

(*Continued on next page*)

Continued

REAGENT or RESOURCE	SOURCE	IDENTIFIER
O_2^- Content Assay Kits	Solarbio Life Sciences	Cat# BC1295
H_2O_2 Content Assay Kits	Solarbio Life Sciences	Cat# BC3595
LPO Content Assay Kits	Solarbio Life Sciences	Cat# BC5245
ROSGreenTM H_2O_2 Probe	MaokangBio	Cat# MX5602-1MG
TUNEL Apoptosis Assay Kit	Beyotime Biotechnology.	Cat# C1088
Deposited data		
miRNA-seq and RNA-seq data	This paper	PRJNA1056442
Proteomics data	This paper	PXD048582
Experimental models: Cell lines		
Mouse neural stem cells (C17.2)	Anwei Biotechnology	AW-CELLS-M0022
Human neural stem cells (ReNcell CX)	Tongwei Biotechnology	C1158
RGC cells	Procell Life Sciences & Technology Co., Ltd	CP-M112
Müller cells	Procell Life Sciences & Technology Co., Ltd	CP-M117
661W	Tongpai Biotechnology	N/A
Experimental models: Organisms/strains		
C57BL/6J	SPF Biotechnology	N/A
Bama miniature pigs	Shoukelingfu Biotechnology	N/A
Software and algorithms		
GraphPad Prism 9.0.0	GraphPad Software Inc.	https://www.graphpad.com/
ImageJ	ImageJ Software Inc.	https://imagej.nih.gov/ij/index.html
BioRender	BioRender	https://www.biorender.com/

EXPERIMENTAL MODEL AND STUDY PARTICIPANT DETAILS

Human samples

We examined the oxidative stress characteristics of vitreous humor samples from the RVO cohort and selected patients with idiopathic macular epiretinal membrane or idiopathic macular holes as a control group, because these patients had lower ROS levels and were able to provide stable baseline data. In addition, these patients allow for the legal collection of vitreous fluid during routine clinical procedures, which meets ethical requirements.[62,63] Meanwhile, we had excluded patients with antioxidant use in these diseases. Collection and measurement of vitreous humor samples were approved by the Ethics Committee of Beijing Chaoyang Hospital (Number: 2022-S-75) and informed consent was obtained from all participants. Demographics and clinical features for the control group and RVO group are presented in Tables S1 and S2, respectively.

Cell lines and culture

Mouse neural stem cells (C17.2), human neural stem cells (ReNcell CX) and 661W cell lines were cultured in Dulbecco's modified Eagle's medium containing 10% fetal calf serum, streptomycin (100 μg/mL) and penicillin (100 U/mL) at 37°C with 5% CO_2, and all the cells were passaged at approximately 80% confluency. The RGC cells were maintained in Neurobasal-A medium (Procell Life Science & Technology Co., Ltd.) containing B-27 supplements and 1% penicillin-streptomycin solution at 37°C with 5% CO_2. The Müller cells were cultured in Müller cell complete medium (Procell Life Science & Technology Co., Ltd.) at 37°C with 5% CO_2. All cell lines were regularly tested negative for mycoplasma by PCR.

Animal models

The mouse experiments were approved by the Institutional Animal Care and Use Committee at the Institute of Process Engineering, Chinese Academy of Sciences (Number: IPEAECA2022063). The miniature pig experiments were approved and performed in accordance with the institutional guidelines of the Experimental Animal Ethics Committee of Shoukelingfu (Beijing) Biosciences (Number: SKLF-DWLL-20221105).

Given that RIRI is a common pathological process in various retinal diseases, including RVO and other ischemic retinal conditions, we established RIRI models in both mice and pigs. Here, RIRI models were induced using anterior chamber perfusion. C57BL/6J mice (6–8 weeks, female, weighing 20 ± 1 g) were purchased from SPF Biotechnology. The mice were housed in an environmentally controlled room (23°C, 55% ± 5% humidity, 12 h: 12 h light: dark cycle). Considering that H_2O_2 levels significantly increase 12 h post-reperfusion, while apoptosis occurs at 24 h, intervening at the 12 h mark allows for effective clearance of H_2O_2 and the prevention of

apoptosis. The mice were anesthetized using an intraperitoneal injection of pentobarbital sodium (50 mg/kg), followed by pupil dilation with compound tropicamide eye drops and corneal surface anesthesia with oxybuprocaine hydrochloride eye drops. A 30 G infusion needle connected to a reservoir of sterile 0.9% saline by silicone tubing was inserted into the anterior chamber. Intraocular pressure was raised to 110 mmHg for 60 min by elevating the saline reservoir to 150 cm. Retinal ischemia was confirmed by the pallor of ocular fundus. After 60 min, the needle was removed and the reperfusion of retinal vessels was confirmed by ophthalmoscopy. Subsequently, mouse eyes were fixed in fixative solution overnight, and embedded in paraffin. Sections (5 μm) of the pupil-to-optic nerve block were cut. After removing the paraffin, H&E staining was performed to verify the successful establishment of the RIRI mouse model. In the sham operation group, a needle was inserted into the anterior chamber without saline infusion.

Bama miniature pigs (4 months, male, weighing 12.5 ± 0.5 kg) were purchased from Shoukelingfu Biotechnology. The pigs were anesthetized using the combined anesthesia of injection (Zoletil®50, 5 mg/kg) and inhalation (2% isoflurane). The operation was the same as in mice, except that the height of the saline reservoir was 170 cm. To ensure the consistency of model, mice or pigs were fed under the same conditions and related experiments were carried out by a single technician throughout the whole period.

METHOD DETAILS

Collection of vitreous humor samples

Vitreous humor samples from patients with RVO, idiopathic macular epiretinal membrane, or idiopathic macular hole were collected using a sterile syringe during vitrectomy (0.1 mL). The vitreous humor samples from RIRI model pigs were collected using a sterile syringe with a 30 G needle (0.05 mL). Three samples of biological repeats were quantified in each group.

Measurement of vitreous humor samples

Vitreous humor samples were frozen in −80°C until assayed. The antioxidase activities (SOD, CAT, GPX) and ROS (O_2^-, H_2O_2, LPO) concentrations were measured using Micro Antioxidase Activity Assay Kits and ROS Content Assay Kits.

Bioinformatics analysis of antioxidase in retinas

The retinal gene expression dataset was downloaded from the Human Protein Atlas (https://www.proteinatlas.org/). All genes with molecular functions classified as peroxidases were analyzed. These genes were then categorized according to their substrate types, and the three most highly expressed categories—GPX, SOD, and CAT—were selected for subsequent analysis.

Measurement of antioxidase and ROS in retinal samples

The Sham and RIRI model mice were killed after 24 h of reperfusion, and the retinas were carefully peeling off under a stereomicroscope. The antioxidase activities (SOD, CAT, and GPX) and ROS (O_2^-, H_2O_2, LPO) concentrations of retinal samples were measured according to the manufacturer's instructions.

Analysis of oxidative stress damage in retinas

The eyeballs of RIRI model mice were fixed in fixative solution overnight, and then embedded in paraffin after dehydration and transparency. Sections (5 μm) of the pupil-to-optic nerve block were cut. We used anti-CAT antibodies (dilution 1:100) for immunohistochemical analysis. After incubation with HRP-labeled secondary antibodies, the immune complexes were visualized using a microscope. The mice were routinely anesthetized after 12 h of reperfusion, and then we injected ROSGreen H_2O_2 Probe (2 μL) into the vitreous cavity using a Hamilton 30 G microinjector. After 30 min, the accumulation of H_2O_2 in murine retinas was visualized using a two-photon fluorescence microscope. The eyeballs of RIRI model mice were collected after 0 h, 24 h, or 48 h of reperfusion, and stored in the optimum cutting temperature compound at −20°C. The frozen eyeballs were further cut into 10 μm tissue sections using a frozen microtome (Leica). The sections were imaged using CLSM (Nikon) to detect TUNEL-positive cells.

Western blot analysis

The total proteins of RGC, Müller, and 661W cells were extracted using RIPA lysis buffer containing 1% PMSF. The protein concentrations cells and exosomes were quantified using bicinchoninic acid assay. Cell or exosome samples were loaded onto a 4–15% SDS-PAGE gel according to the manufacturer's instructions. For immunodetection, the gels were transferred onto immunoblot polyvinylidene fluoride membranes (Biosharp) by wet transfer and subsequently blocked. The expressions of ALIX, CD63, TSG101, SOX2, Nestin, CAT, and β-actin were evaluated by western blotting with equal loading protein dose (20 μg). Goat anti-rabbit IgG H&L (HRP), goat anti-mouse IgG H&L (HRP), and immobilon western chemiluminescent horseradish peroxidase substrate (Millipore) were used for chemiluminescence detection of proteins. The gels were imaged using the GelDoc Go gel imaging system (Bio-Rad).

Construction of CataKNexo

The lentiviral fusion plasmids (pLVX-puro-CD63-CAT, mouse or human) were synthesized by BGI Genomics Co., Ltd. The lentiviral solution was then produced using the plasmid according to the manufacturer's instructions. Lentiviral solution (1 mL) was added into C17.2 or ReNcell CX cells (60% density) with polybrene (2 μg/mL). After 24 h of culture, the medium containing lentivirus was replaced with fresh medium, and the positive transfected cells were screened by puromycin (2 μg/mL). The above cells were cultured with

exosome-free serum to isolate exosomes expressing CAT. Exosomes were prepared according to a typical protocol. Briefly, culture supernatant containing 1×10^7 cells (from C17.2 or ReNcell CX) was centrifuged at 300 g or 2,000 g for 10 min to remove cells and cell fragments, respectively. The obtained supernatant was centrifuged at 10,000 g for 30 min at 4°C to remove debris. The final supernatant was then ultracentrifuged at 100,000 g for 70 min twice to obtain a pellet containing exosomes. The obtained exosomes were resuspended in PBS containing approximately 0.15 mg of protein. All batches of exosomes were isolated strictly using the standardized methods described above. Next, EDC and NHS (5 mg, respectively) were added into the PBS containing exosomes (20 μL). After reacting at 37°C for 1 h to activate the carboxyl on the surface of exosomes, K_{10} peptides (2 mg) were added. Then lysine were stably conjugated to the surface of exosomes through condensation reaction after reacting at 37°C for 2 h. Exosome centrifuge columns were used to remove excess EDC, NHS, and unreacted lysine to obtain CataKNexo.

Characterization of CataKNexo

Images of CataKNexo stained with uranyl acetate were obtained using a JEM-1400 TEM (Jeol). The size and zeta potential were determined using nanoparticle tracking analysis (NTA, Particle Metrix).

Co-localization of CataKNexo

We labeled CAT with fluorescent secondary antibody (Cy3) and lysine with FITC, respectively. Double-labeled CataKNexo were immobilized on a confocal dish and visualized using CLSM and STED (SP8, Leica) for fluorescent imaging.

CAT activity and H_2O_2 scavenging analysis

CAT activities of Nexo (10 μg), CataNexo (10 μg), and CataKNexo (10 μg) were measured using CAT Activity Assay Kit according to the manufacturer's instructions. Absorbance values of H_2O_2 were determined at different time points for comparing the H_2O_2 scavenging efficiency of CataKNexo and commercial catalase.

Agarose gel electrophoresis analysis

Exosomes labeled with PKH26 were added to 0.3% agarose gel. Electrophoresis was carried out at 100 V for 30 min, and the gel was imaged using the GelDoc Go gel imaging system.

Proteomic and miRNA-sequencing analysis

The fresh and Lyo/Reh CataKNexo were sent to Personalbio for label-free quantitative proteomic and miRNA-sequencing analysis. Briefly, the total proteins of CataKNexo were extracted using RIPA lysis buffer. The proteins were subsequently cleaved and the peptides were extracted for detection using liquid chromatography-tandem mass spectrometry. Finally, the alignment analysis was performed according to the protein database. miRNA sequencing was performed according to a typical protocal using the Illumina sequencing platform.

Intravitreal injection

After RIRI model mice were anesthetized, we injected PBS, CAT, Nexo, CataNexo, CataKNexo, Nerve Growth Factor (NGF) + N-acetyl-L-cysteine (NAC), or CAT+Nexo into the vitreous cavity using a Hamilton 30 G microinjector. The single injection dose per eye was 2 μL of PBS, 10 μg of exosomes, 5 μg of NGF and NAC, and 2 μg of CAT. We injected PBS or CataKNexo into the vitreous cavity using a sterile syringe with a 30 G needle after RIRI model pigs were anesthetized. The single injection dose per eye was 50 μL of PBS and 250 μg of CataKNexo.

Imaging of nanodrug distribution

We injected CAT, Nexo, CataNexo, or CataKNexo labeled with Cy5-SE into the vitreous cavity of RIRI model mice and imaged at different time points using the *in vivo* imaging system (IVIS, Kodak) with the Carestream MI software (v.5.0.7). After 24 h of injection, the eyeballs were isolated for further imaging. The filter was as follows: excitation 647 nm and emission 700 nm, exposure time 30.0 s. For the detection of Cy5-SE-labeled exosomes, the link checkbox was set as 'Select All', and the display lookup table selected was 'Rainbow'. The regions of interest (ROIs) in the fluorescence images were drawn using the parameter settings of 'Manual-ROIs', and were quantified by selecting the 'ROI Rectangle' option to identify the regions. After 48 h of injection, the RIRI model pigs were euthanized using an intravenous injection of pentobarbital sodium (100 mg/kg). The eyeballs were isolated and imaged using the IVIS. The filter setting and image processing were the same as above.

Multi-stage targeting ability

Retinal frozen sections from mice subjected to 24 h of reperfusion were labeled using immunofluorescence of anti-SDF1 antibody. The sections were subsequently imaged using CLSM. The CXCR4 chemokine receptors were blocked after the incubation of CataKNexo with anti-CXCR4 antibody at 4°C overnight. We injected PKH26-labeled CataKNexo with or without blocking into the vitreous cavity using a Hamilton 30 G microinjector. After 24 h of injection, mice were perfused systemically and the eyeballs were isolated for transparency according to the CUBIC (TCI) protocol. Briefly, the eyeballs were preprocessed using CUBIC-L solution in 37°C for 24 h. Then the eyeballs were degreased using CUBIC-L solution in 37°C for 5 days (replaced CUBIC-L solution every

2 days). Nuclei were stained with DAPI solution at room temperature for 3 days. CUBIC-R+ solution were applied at room temperature for pretreatment. Finally, the eyeballs were matched using CUBIC-R+ solution at room temperature for 1 day and imaged using LSFM to observe the primary targeting of CataKNexo.

The eyeballs of mice and pigs used in the IVIS were cut into 10 μm tissue sections using a frozen microtome. The sections were further stained with DAPI and imaged using CLSM to observe the secondary targeting of CataKNexo.

Construction of iterative Transwell co-culture model

The upper chamber of 24-well Transwell plate (pore size of 3 μm, Corning) was placed on the upper chamber of 12-well Transwell plate to construct the iterative Transwell plate. The top layer was loaded with 5×10^4 RGC in 200 μL of DMEM, the middle layer was loaded with 1×10^5 Müller cells in 500 μL of DMEM, and the bottom layer was loaded with 1×10^6 661W cells in 1 mL of DMEM. We selected Müller cells for constructing our *in vitro* model due to their crucial role in the INL and the availability of a stable primary culture method. The iterative Transwell co-culture model was subsequently induced with OGD/R. Taking 661W as an example, our experimental results showed significant H_2O_2 elevation and cell apoptosis after OGD/R treatment, aligning with the phenomenon observed by *in vivo* ischemia-reperfusion injury. Then we added PKH26-labeled Nexo, CataNexo, and CataKNexo into the top layer. After 24 h of incubation, the cytoskeleton was labeled with FITC-Phalloidin and imaged using CLSM.

In vitro targeting mechanism analysis

RGC of the top layer were collected to analyze the endocytosis of Nexo, CataNexo, and CataKNexo using flow cytometry. In addition, the indicated inhibitors for distinct endocytosis pathways were applied to analyze the most dominant endocytosis pathway of CataKNexo in RGC. The lysosomes and Golgi apparatus were labeled with Lyso-Tracker Green and Golgi-Tracker Green, and then imaged using CLSM.

Au nanoparticles (10 nm) were prepared using the typical protocol of reducing chlorauric acid with sodium citrate. Au nanoparticles were added in the culture of positive transfected neural stem cells to obtain Au nanoparticles-labeled CataKNexo. After 24 h incubation of Au nanoparticles-labeled CataKNexo with RGC, images of RGC stained with uranyl acetate were obtained using a JEM-1400 TEM.

Cell phenotypes and safety analysis of 661W cells after treatment with CataKNexo

Changes in cell phenotype (Nestin, Opn1mW, γ-synuclein, and βIII-Tubulin) were analyzed by CLSM after incubating 661W cells with CataKNexo for 24 h. Cell viability analysis: 661W cells were seeded in 96-well plates. After the cells adhered to the surface and reached 40%–50% confluence, different concentrations of CataKNexo (1 μg, 5 μg, and 10 μg) were added. Six replicates were performed for each group. The cells were cultured for about 24 h, and the cell phenotype was observed under a microscope on the following day. Subsequently, CCK-8 assay kit was added into each well and incubated at 37°C for 2–4 h. The absorbance at 450 nm was measured using an enzyme marker and the cell viability of each group was calculated based on the absorbance value.

RNA-sequencing analysis

Collected retina tissues of mice were fast frozen in liquid nitrogen and then sent to Gene *Denovo* Biotechnology for sample preparation and detection. Briefly, RNAs were purified from the retinal tissues of mice and reverse-transcribed using SuperScript III reverse transcriptase according to the manufacturer's instructions. The cDNAs were sonicated using a Covaris S2 ultrasonicator, and the libraries were prepared using the KAPA high-throughput library preparation kit. All libraries were sequenced using the BGISEQ-500 sequencing platform. The expression levels of RNAs were determined using the fragments per kilobase of transcript per million mapped reads method. The fold-change method was used to identify RNAs that were differentially expressed after castration using the R package DESeq2 (v.1.24.0). Genes with a log2 fold change >2 and an adjusted $p < 0.05$ were deemed to be significantly differentially expressed.

Transcytosis scoring

Bioinformatics was employed to analyze the transcytosis of 661W and Müller cells. Transcriptome data for 661W (ID: GSM6603348, $n = 6$) and Müller cells (ID: GSM7635142, $n = 4$) were downloaded from the GEO database. Both datasets were preprocessed using FPKM normalization, and for genes with multiple probes, the mean value was used to replace individual probes. The two datasets were then merged, and batch effects were removed using the ComBat method from the sva package. Finally, the GSVA package was used to score gene expression within the Gene Ontology term ''transcytosis (GO: 0045056)''.

Histopathology analysis

The eyeballs of mice or pigs were collected after the administration of 36 h or 72 h, and stored in the optimum cutting temperature compound at −20°C. The frozen eyeballs were further cut into 10 μm tissue sections using a frozen microtome. Retinal frozen sections of mice were labeled using immunofluorescence of anti-βIII-Tubulin antibody, and then imaged using CLSM. The sections of mice and pigs were imaged using CLSM (Nikon) to detect TUNEL-positive cells.

The eyeballs of pigs were fixed in fixative solution overnight, and embedded in paraffin after dehydration and transparency. Sections (5 μm) of the pupil-to-optic nerve block were cut. HE staining was performed after deparaffinization, and the sections were visualized using a microscope.

PCR

Total RNAs were extracted from the retinal tissues of pigs using RNAeasy Animal RNA Isolation Kit with Spin Column. The primers of pig GAPDH and βIII-Tubulin were listed as follows: GAPDH forward 5′-GCAAAGTGGACATTGTCGCCATCA-3′, reverse 5′-AGCT TCCCATTCTCAGCCTTGACT-3'; βIII-Tubulin forward 5′-CAGCAAGGTGCGTGAGGAGTAT-3′, reverse 5′-GTGGTTGAGGTCCCCG TAGG-3'. The qRT-PCR analysis was conducted using BeyoFast SYBR Green One-Step qRT-PCR Kit on the platform of CFX96 Touch Real-Time PCR Detection System (Bio-Rad). The relative abundance of βIII-Tubulin was normalized by the level of GAPDH mRNA expression.

Electroretinography

The full-field electroretinogram (ERG) is an effective method for characterizing visual function in mice.[64] After 36 h or 72 h of administration, the mice or pigs were placed in a dark room for dark adaptation of 2 h. The mice or pigs were routinely anesthetized followed by pupil dilation and corneal surface anesthesia. The negative electrode was inserted into the eyelid and the positive electrode was positioned on the surface of cornea. The maximum mixed response of dark adaptation 3.0 was recorded using the visual electrophysiology instrument (HealthOLight Technology) after the oscilloscope showed a stable display.

Optical coherence tomography

After 72 h of the treatment with PBS or CataKNexo, the thickness of porcine retinas was imaged and analyzed using the ultramicroscopic imaging system (HealthOLight Technology).

Safety assessment *in vivo*

Intraocular pressure of mice and pigs were measured using tonometers (Icare Tonolab). CBC and blood biochemistry of mice and pigs were performed using DxH900 hematology analyzer (Beckman Coulter) and AU480 chemistry analyzer (Beckman Coulter). Color fundus photography of pigs was conducted using the retinal imaging system (HealthOLight Technology).

QUANTIFICATION AND STATISTICAL ANALYSIS

Statistical analyses were performed using GraphPad Prism 9.0.0 software. All graphs present mean ± S.D., unless otherwise specified. A two-tailed unpaired Student's t test or Mann-Whitney U-test was used to compare two groups, and one-way ANOVA analysis of variance was used to compare multiple groups. The correlation was analyzed by Spearman's rank correlation or Pearson correlation analysis. The threshold for statistical significance was set at $p < 0.05$.